Oligomerization and feedback on membrane recruitment stabilize PAR-3 asymmetries in *C. elegans* zygotes.

Charles F Lang[1,2,4], Alexander Anneken[1], and Edwin M Munro[1,2,]

1 *Department of Molecular Genetics and Cell Biology, University of Chicago, Chicago, IL 60637*
2 *Committee on Genetics, Genomics and Systems Biology, University of Chicago, Chicago, IL 60637*
3 *Institute for Biophysical Dynamics, University of Chicago, Chicago, IL 60637*
4 *Current address: Department of Molecular and Cellular Physiology, Stanford University, Stanford, CA 94305*
5 *Correspondence to emunro@uchicago.edu*

Contact info:
Edwin Munro
Molecular Genetics and Cell Biology
University of Chicago
920 E 58th St
CLSC 901
Phone: (773)-702-6221
Fax: (773) 702-3172
email: emunro@uchicago.edu

Abstract

The PAR polarity network is a paradigmatic example of how systems of mutually antagonism interactions among peripheral membrane binding proteins allow them to form and maintain complementary polar domains in response to a transient polarizing cue. The oligomeric scaffolding protein PAR-3 has emerged as a keystone member of the PAR network in many different contexts. In early *C. elegans* embryos, PAR-3 is required for all other PAR asymmetries, and it can form stable unipolar asymmetries when its known inhibitors are absent and all other members of the PAR network are cytoplasmic or spatially uniform on the membrane. But how PAR-3 forms stable unipolar asymmetries absent mutual antagonism is unknown. Here we combine single particle analysis with quantitative modeling and experimental manipulations to determine how the dynamics of PAR-3 membrane binding, oligomerization and dissociation allow PAR-3 to maintain stable asymmetries in the one cell *C. elegans* embryo. We find that two forms of positive feedback contribute to sustaining PAR-3 asymmetries: First, a sharp size-dependent decrease in oligomer dissociation rates makes the effective dissociation rate of PAR-3 decrease sharply with its membrane density. Second, membrane-bound PAR-3 promotes additional binding of PAR-3 to the membrane through a mechanism that requires the presence of anterior polarity proteins CDC-42, PAR-6 and PKC-3. Through a combination of modeling and quantitative measurements, we show that these two feedback loops are sufficient to dynamically stabilize asymmetries of the magnitude observed in polarized *C. elegans* zygotes. These results establish a dynamic basis for stabilizing monopolar PAR-3 asymmetries; they underscore a crucial role for the oligomerization and add to the growing body of evidence that point to a central role for oligomerization of peripheral membrane proteins in the establishment and maintenance of cell polarity.

Introduction

The PAR proteins are a highly conserved network of proteins that govern cell polarity in many different cells and tissues across the metazoa [1,2]. In all of these contexts, the PAR proteins become asymmetrically enriched in response to transient local cues. These asymmetries are reinforced through feedback loops in which PAR proteins locally promote or inhibit one another's accumulation. Asymmetrically enriched PARs then act through different downstream targets to elaborate functionally polarized states. While the local polarizing cues vary widely across different contexts, the interactions among PAR proteins that govern the response to these cues is more highly conserved. Thus, a central challenge is to understand how systems of feedback among the PARs encode their ability to form and stabilize spatial patterns of enrichment that define functional polarity.

The one-cell *C. elegans* embryo, (a.k.a. the zygote), has been a powerful model system for uncovering the core molecular circuitry that governs PAR polarity. During polarization of the zygote, two sets of PAR proteins become asymmetrically enriched in complementary anterior and posterior membrane domains. The anterior aPARs include the oligomeric scaffold PAR-3, the adaptor PAR-6, the kinase PKC-3, and the small GTPase CDC-42. The posterior pPARs include the kinase PAR-1, a *C. elegans*-specific protein called PAR-2, and a putative CDC-42 GAP called CHIN-1.

Polarization proceeds through two distinct phases, called establishment and maintenance [3], which correspond respectively to mitotic interphase and mitosis. Before polarization, aPARs are uniformly enriched at the cell surface, while pPARs are largely cytoplasmic. During polarity

establishment, a local sperm-derived cue triggers the redistribution of aPARs and pPARs into complementary domains. The sperm cue is closely associated with a centrosomal microtubule organizing center called the sperm MTOC that forms near the site of sperm entry [4,5]. The sperm MTOC acts through the aurora kinase AIR-1 [6–9] to trigger actomyosin-based cortical flows that transport aPARs towards the anterior pole [10,11]. In addition, astral microtubules associated with the sperm MTOC promote the local accumulation of pPARs PAR-1 and PAR-2 on the posterior cortex [12,13].

During mitosis, the centrosomes (thus the polarity cue) migrate to the cell center. However, PAR asymmetries are maintained through mitosis despite continuous diffusion and exchange of PAR proteins between the cytoplasm and the cell membrane [14,15]. The prevailing model is that PAR asymmetries are maintained by a network of mutually antagonistic interactions in which aPARs and pPARs act locally to inhibit one another's accumulation (reviewed in Lang and Munro [2], Figure 1A). Both PAR-3 and active CDC-42 are required for local recruitment of PAR-6/PKC-3 into an active complex with CDC-42 [16,17]. Active PKC-3 inhibits local accumulation of pPARs, including PAR-1 and CHIN-1 [12,16,18–22]. PAR-1 inhibits local accumulation of PAR-3 [12,23], while CHIN-1 inhibits local activation of CDC-42 [16,22,24]. Because both PAR-3 and CDC-42 are required for local recruitment of PAR-6/PKC-3 during mitosis, either PAR-1 or CHIN-1 is sufficient to prevent posterior recruitment of PAR-6/PKC-3.

Strikingly, cortical PAR-3 asymmetries persist in zygotes that lack both PAR-1 and CHIN-1, even though the aPARs CDC-42, PAR-6 and PKC-3 are uniformly enriched, and the remaining pPARS are cytoplasmic [16] (Figure 1B). PAR-3 is the keystone member of the PAR network

without which all other PAR asymmetries are lost. Segregation of PAR-3 is a first step in polarization in many different contexts [12,25–28] (C. elegans refs, dros, neuroblasts). Thus additional mechanisms must exist to maintain monopolar PAR-3 asymmetries in the absence of mutual antagonism with pPARs and these mechanism must also contribute to shaping PAR symmetries in normal embryos. Importantly, monopolar PAR-3 asymmetries have also been observed under wild type conditions in other contexts, including in neuroblast stem cells [29–31] and in mammalian hippocampal neurons [32] and *Drosophila* male germline cells [33]. However, their molecular bases remain unknown.

A key feature of PAR-3 is its ability to form oligomers at the cell membrane. PAR-3 self-associates through a conserved N-terminal PB1-like domain, called the CR1 domain [34]. The purified CR1 domain assembles head to tail into helical filaments in vitro [35,36]. While PAR-3 contains multiple domains that can support direct binding to plasma membranes [37,38], deletion or mutation of the CR1 domain prevents strong accumulation of PAR-3 in *C. elegans* [37] (and in *Drosophila* and mammalian cells [34,35,38]) and induces defects in embryonic polarity [17,37,39]. Oligomerization of PAR-3 plays an essential role in polarity establishment by coupling PAR-3 to the actomyosin cortex to facilitate segregation of PAR-3 and other aPARs by anterior-directed cortical actomyosin flows [17,26,39–41]. But whether oligomerization of PAR-3 plays additional roles in polarity maintenance, and in particular whether and how oligomerization of PAR-3 might contribute to stabilizing PAR-3 asymmetries in the absence of mutual antagonism, remains unknown.

Here, we combine single molecule imaging and particle tracking analysis with genetic manipulations and modeling to reveal the basis for self-stabilizing PAR-3 asymmetries in the *C. elegans* zygote. We show that PAR-3 asymmetries are maintained despite continuous rapid exchange of subunits with PAR-3 oligomers. We find that two key factors maintain PAR-3 asymmetries in the absence of posterior inhibition: Size-dependent membrane binding avidity of PAR-3 oligomers confers negative dependence of PAR-3 dissociation rate on local PAR-3 density – a form of positive feedback. Second, enhanced recruitment of PAR-3 to membranes where PAR-3 is already enriched, which depends on aPARs CDC-42, PAR-6 and PKC-3, provides a second form of positive feedback. Mathematical models, tightly constrained by our experimental measurements, show that the combination of size-dependent binding avidity and enhanced recruitment are sufficient to ensure dynamically stable PAR-3 asymmetries. We show further that sharp dependence of PAR-3 oligomer mobility on size ensures that the boundaries of PAR-3 domains are effectively stable in the absence of cortical flow, while remaining sharply responsive to patterns of flow. Thus, self-stabilizing PAR-3 asymmetries encode a lasting memory of PAR distributions shaped by cortical flow. Together, these results reveal a novel mechanism for stabilizing PAR-3 asymmetries in the absence of mutual antagonism, which depends on core dynamics of PAR-3 oligomer assembly and interactions with its conserved partners CDC-42, PAR-6 and aPKC. We propose that similar mechanisms may underlie the stabilization of unipolar PAR asymmetries in other contexts.

Results

PAR-3 asymmetries approach a plateau during maintenance phase.

As a first step towards characterizing the mechanisms that maintain PAR-3 asymmetries in the absence of posterior inhibition, we used near-TIRF microscopy and single particle analysis to quantify dynamic changes in PAR-3 oligomer size and density during polarization in homozygous *par-1* mutant embryos, using background-subtracted intensity as a proxy for mean oligomer size (Figure 2A-D, Movie S1, see Methods). Consistent with previous reports [39,40], mean oligomer size, number density and overall density of PAR-3 density increased steadily on the anterior cortex and decreased on the posterior cortex during polarity establishment phase as cortical flows transport PAR-3 towards the anterior pole. At the onset of maintenance phase, both mean oligomer size and overall density of PAR-3 began to decrease, driven at least in part by phosphorylation of PAR-3 by POLO Kinase PLK-1 [39]. However, the density of PAR-3 oligomers remained approximately constant through maintenance phase, while the rate of decrease in mean oligomer size and overall PAR-3 density slowed progressively, such that both approached plateau levels in late maintenance, representing ~50% of their maximum levels during establishment phase. We observed similar changes in mean oligomer size and density on the anterior cortex of control (*par-1* heterozygote) embryos and throughout the cortex in embryos depleted of SPD-5 by RNAi, which lack a functional sperm cue and fail to establish polarity (Figure S1). Thus maintenance of PAR-3 asymmetries in both wild type and *par-1* mutant embryos appears to involve the dynamic approach to steady state, characterized by stably asymmetric distributions of PAR-3 oligomers.

Oligomerization and size-dependent oligomer dissociation induces positive feedback on PAR-3 accumulation to reinforce PAR-3 asymmetries.

To determine the kinetic basis for maintenance of PAR-3 asymmetries, we turned to single molecule imaging and particle tracking analysis. As a framework for this analysis, we considered a simple model for membrane binding and oligomerization of PAR-3 in which: (a) cytoplasmic PAR-3 monomers bind reversibly to the plasma membrane where they associate reversibly to form PAR-3 oligomers, (b) cytoplasmic PAR-3 monomers bind directly and reversibly to membrane-bound PAR-3 oligomers and (c) membrane-bound PAR-3 oligomers undergo size-dependent dissociation (Figure 3A) As we previously showed (Lang and Munro, 2022), this simple model makes several basic predictions, conditioned on the kinetics of PAR-3 oligomer dissociation: First, at steady state, the model predicts a monotonically decreasing distribution of oligomer sizes (Figure 3B). If oligomers dissociate much more slowly than monomers, this distribution approximates an exponential distribution given by $P_n = P_1\alpha^{n-1}$, with mean oligomer size $s = \frac{1}{1-\alpha}$, where P_n is the density of oligomers with n subunits and α is a measure of oligomerization strength that depends on binding/unbinding rates and the pool of available subunits (see Methods, Lang and Munro, 2022 [42] for details). Second, the model predicts that mean oligomer size should increase with total density of membrane bound PAR-3; if oligomers dissociate more slowly than monomers, this implies a form of positive feedback in which the effective off-rate due to unbinding of PAR-3 monomers and oligomers from the membrane, defined as: $k_{eff}^{diss} = \frac{\sum nPk_{off}(n)}{\sum nP_n}$, decreases with overall density of membrane-bound PAR-3 (Figure 3C). We will refer to this below as positive feedback through size-dependent oligomer dissociation.

To test these predictions, we first measured the distributions of PAR-3 oligomer sizes on anterior and posterior membranes in *par-1* mutant embryos during late maintenance phase, when the densities of PAR-3 have reached a plateau. We used embryos expressing endogenously-tagged PAR-3::GFP, and we used the intensities of single PAR-3::GFP molecules, measured in the same embryos after photobleaching, as an internal size standard (Figure 3D-F, see Methods). Consistent with our model's predictions, both the anterior and posterior distributions of oligomer sizes approximated an exponential distribution Both oligomerization strengths ($\alpha_A = 0.730 \pm 0.052$, $\alpha_P = 0.424 \pm 0.054$) and mean oligomer sizes ($s_A = 3.48 \pm 0.65$, $s_P = 1.65 \pm 0.16$) were higher on the anterior cortex where total PAR-3 density is higher (Figure 3G-I) We also confirmed the positive dependence of PAR-3 oligomer size on total density in embryos depleted of PAR-3 to different extents (see below and Figure 5D).

To estimate the size-dependence of PAR-3 oligomer dissociation, we performed fast imaging and particle tracking analysis of mNG::PAR-3, using the mean intensities of single molecules to calibrate estimates of oligomer size, as described above (Figure 3J; see Methods). To improve the accuracy of particle tracking, we performed these experiments in embryos depleted of the Myosin II heavy chain NMY-2 by RNAi, which increases the distance between particles by preventing the segregation of PAR-3 to the anterior pole during polarity establishment and eliminates the movements of particles driven by local actomyosin contractility (Figure 3J) We used the intensities of oligomers in the first frame of the imaging sequence (before photobleaching occurs) to estimate oligomer size and then used the fraction of oligomers in each size class with bound lifetimes > 1 sec to estimate a first-order dissociation rate constant. The estimated dissociation rate constants for PAR-3 oligomers decreased sharply with oligomer size,

becoming negligible for oligomer sizes > 3 subunits (Figure 3K). These data confirm the existence of positive feedback due to size-dependent oligomer dissociation. We found that they could be fit quite well by $k_{off}(n) = 3\beta^{n-1}$ with $\beta = 0.25$. Using this fit and our estimates of oligomerization strengths $\alpha_A = 0.73$ and $\alpha_P = 0.424$ (see Methods), we estimated that this feedback produces a 3.8-fold A:P difference in the effective dissociation rate of PAR-3, accounting for roughly half of the asymmetry observed in late maintenance phase.

Rapid exchange of PAR-3 monomers with the membrane and with membrane-bound oligomers underlies maintenance of PAR-3 asymmetries.

Next, we quantified the PAR-3 exchange kinetics that underly the apparent steady state observed in late maintenance phase, using two complementary approaches. First, we used embryos expressing transgenic PAR-3::GFP to measure rate constants for dissociation of single PAR-3 molecules from the membrane or from PAR-3 oligomers. From our measurements of PAR-3 oligomer size distributions, we infer that the majority of PAR-3 molecules on the anterior cortex are associated with PAR-3 oligomers, which undergo slow sub-diffusive motion (Sailer et al, 2015 [16], Chang and Dickinson 2022 [26], see below), while the majority of single molecules observed on the posterior cortex are associated with PAR-3 monomers, which undergo rapid Brownian diffusion. This allowed us to optimize strategies to image and accurately track sparsely-labelled pools of membrane- or oligomer-bound PAR-3::GFP molecules (Figure 4A,B, Robin et al, 2014 [15], see Methods) and to infer dissociation rate constants from release curves plotting the percentage of molecules with observed lifetimes > t sec for different values of t (Figure 4C-E).

For anterior molecules with lifetimes t > 200 msec, the distribution of root mean squared displacements after 200msec were consistent with slow subdiffusive motion (Figure 4B, right), and the release curves were well-fit by single exponentials (Figure 4C, right). These data are consistent with a population of PAR-3 molecules bound to PAR-3 oligomers that disappear with a single observed rate constant for disappearance k_{obs}, which is the sum of an intrinsic dissociation rate constant k_{diss} and a photobleaching rate constant k_{pb}. Measuring k_{obs} for different exposure duty ratios (dr; Figure 4D , Methods), and fitting the data to $k_{obs} = k_{diss} + k_{pb} * dr$, produced separate estimates of rate constants for photobleaching (k_{pb}= 1.04/s) and dissociation (k_{diss}= 0.08/s ; Figure 4E; Methods).

For posterior molecules with bound lifetimes t > 200 msec, the distribution of root mean squared displacements were consistent with Brownian diffusion at 0.12 µm^2/sec (Figure 4B, left), and release curves were consistent with a single dominant rate constant for disappearance (Figure 4C, left). Correcting for photobleaching (see Methods) revealed an estimate for the rate constant for dissociation of PAR-3 from the membrane (k_{diss}= 2.1/sec), which is smaller than, but consistent with, our measurements of size-dependent dissociation of PAR-3 oligomers in Figure 3K. We measured similar dissociation rates for a transgenically-expressed version of PAR-3 (PAR-3(ΔCR1)::GFP) that lacks the N terminal CR1oligomerization domain (Figure S2C-E).

As a complementary approach to measure the kinetics of PAR-3 exchange, we used near-TIRF illumination to rapidly and partially photobleach the cortical pool of GFP::PAR-3 during early maintenance phase and then monitored the recovery of total GFP::PAR-3 fluorescence on the anterior cortex (Figure 4F), using a time interval (3 sec) much longer than the expected recovery

time for membrane-bound monomers (~0.5sec) to focus on the recovery of fluorescence within oligomers. After correcting for the decrease in PAR-3 intensity observed during early maintenance in unbleached embryos (Figure 2D; see Methods), we observed a rapid partial recovery of total PAR-3 fluorescence to ~ 43% of its original value (Figure 4G) with a mean half-time of 8.52 +\- 4.3 seconds (Figure 4H, n = 4 embryos), in close agreement with our estimates of the mean residence time of single oligomer-bound molecules.

The partial recovery of PAR-3::GFP fluorescence is consistent with the possibility that PAR-3 forms linear oligomers, and that dissociation rate constant measured above for oligomer-bound PAR-3 reflects the exchange of terminal subunits, while internal subunits exchange more slowly. To probe this further, we performed FRAP experiments on embryos stalled in late establishment phase by treatment with *pri-1 RNAi* [43] (Figure S3A,B,), where mean oligomer sizes remain ~constant, and the largest PAR-3 oligomers are brighter, relatively sparse, and thus easy to track at low image acquisition rates (Figure S2C). Under these conditions, we observed more complete FRAP recovery, on average, for individually tracked clusters, but at longer times, and with non-exponential kinetics (Figure S2D).

Inspection of these data also revealed that during recovery, new bright puncta almost never appear on the cortex, suggesting that PAR-3 oligomers assemble locally on the cell membrane, rather than assembling in the cytoplasm and then binding to the membrane. To confirm this, we analyzed the same fast imaging data used to measure oligomer dissociation rates (Figure 3J,K) and inferred the number of molecules in PAR-3 particles that appear de novo in the imaging plane, representing newly-bound PAR-3 particles. We found that the fluorescence intensity

distribution of these newly detected particles almost exactly matches the distribution of single mNG::PAR-3 molecules, suggesting that PAR-3 binds to the membrane in monomeric form and that oligomerization occurs primarily at the cell membrane.

Finally, we asked if the measured kinetics of oligomer turnover could explain the slow relaxation to steady state observed during maintenance phase. We constrained the simple model (Figure 3A) using our measurements of monomer and oligomer dissociation rates and mean oligomer size, then simulated the approach to steady state from a distribution of oligomer sizes representing late establishment phase. We observed reasonably good agreement between observed and simulated time courses of decrease in oligomer size and density. Together, these results show that during maintenance phase, in the absence of posterior inhibition, PAR-3 asymmetries approach a dynamic steady state which is maintained in the face of continuous rapid exchange of PAR-3 monomers with the plasma membrane and with a pool of more stably bound PAR-3 oligomers.

Positive feedback on monomer recruitment contributes to stabilizing PAR-3 asymmetries during maintenance phase.

We have shown that positive feedback due to size-dependent oligomer dissociation contributes to reinforcing PAR-3 asymmetries during maintenance phase. However, this feedback cannot account for the ~7-fold A:P ratio of PAR-3 densities observed at steady state in *par-1* mutant embryos. Moreover, theoretical analysis of the simple kinetic model in Figure 3A shows that this form of feedback is insufficient by itself to stabilize an asymmetric distribution of membrane bound oligomers [42]. We therefore asked whether there is also positive feedback on PAR-3 recruitment. To test this possibility, we used fast single molecule imaging to measure rates of

single molecule recruitment on anterior and posterior membranes during maintenance phase in wild type and *par-1* mutant embryos (Figure 5A). In these experiments, single molecule speckles appear on the membrane and then rapidly disappear as they unbind or photobleach, allowing us to detect and count a large number of appearance events per unit area and time. To avoid the confounding effects of direct binding of cytoplasmic PAR-3 to membrane-bound oligomers, we performed these measurements on a variant of PAR-3 (PAR-3(ΔCR1)::GFP that lacks the conserved N-terminal CR1 domain that mediates homo-oligomerization [34,35,37]. To avoid counting cytoplasmic molecules that diffuse into the focal plane, we focused on molecules with tracked lifetimes > 200 msec, for which distributions of rmsd at 200 msec matched those expected for membrane-bound PAR-3 molecules undergoing Brownian diffusion. From release curves for these molecules, we extrapolated the number of membrane binding events with bound lifetimes < 200msec (see Methods). We found that during maintenance, single PAR-3 (ΔCR1) molecules bound the membrane bound the anterior membrane on average 2.5 times more frequently than posterior membranes in wild type embryos and 2.0 times more frequently in *par-1* mutant embryos (Figure 5B). Importantly, taken together, the A:P ratios in effective dissociation rate (3.8) and recruitment rate (~2) are sufficient to account for the total PAR-3 asymmetry observed in late maintenance phase.

We then used simulations to ask: If the asymmetry in recruitment represents positive feedback, is the strength of feedback sufficient to ensure dynamically stable PAR-3 asymmetry? We introduced a simple form of feedback into our model, in which the monomer recruitment rate is the sum of a basal rate and a rate that is proportional to the local density of PAR-3 subunits (cyan arrow in Figure 5C). We sampled different values for mean oligomer size s and feedback

strength k_{fb}, defined as the ratio of the monomer binding rate measured at the spatially uniform steady state to the basal recruitment rate, and used our measurements of monomer and oligomer dissociation kinetics to constrain the values of other kinetic parameters (see Methods). The resulting simulations yield a phase diagram showing how the ability to polarize depends on mean oligomer size s and feedback strength k_{fb}. We used our estimates of mean oligomer size in *par-1* mutant embryos (Figure 3I, s ~ 3.2) and estimates of feedback strength $k_{fb} \sim 1$ based on the measured A:P recruitment ratios (Figure 5B) and the relative intensities of spatially uniform and asymmetrically enriched PAR-3 at late maintenance phase in *spd-5(RNAi)* (Figure S1C,D) and *par-1-* mutant (Figure 2) embryos to locate the maintenance phase embryo in this phase diagram (yellow dot in Figure 5D). The result of this comparison suggests that the combination of feedback due to size-dependent dissociation of PAR- 3 oligomers and positive feedback on monomer recruitment is sufficient to ensure stable PAR-3 asymmetry.

The asymmetric membrane binding of PAR-3(ΔCR1)::GFP is consistent with positive feedback of PAR-3 density on membrane recruitment (cyan arrow in Figure 5C). However, it could also reflect an asymmetric bias on monomer binding that does not depend (directly or indirectly) on local densities of PAR-3 (magenta arrow in Figure 5C). To distinguish these two scenarios, we used simulations to produce two alternative predictions for how the measured asymmetry of PAR-3 should respond to variation in mean oligomer size) produced by varying the total amount of PAR-3 in the system, given a fixed asymmetric bias or positive feedback on recruitment; then we tested these predictions by varying PAR-3 levels in living embryos (Figure 5D,E).

Our simulations predict that a key difference between the two scenarios lies in the PAR-3 asymmetries predicted for low levels of total PAR-3 (compare cyan and magenta curves in Figure 5E). For a fixed two-fold A:P bias in monomer binding, the predicted PAR-3 asymmetries persist as the total PAR-3 approaches 0, approaching a fixed value > 2 (magenta curve in Figure 5E) , which is determined by the combined effects of asymmetric recruitment and the negative dependence of effective dissociation rate on density of membrane-bound PAR-3. In contrast, for positive feedback on membrane recruitment whose strength yields a two-fold difference in recruitment rates at steady state, our simulations predict that PAR-3 asymmetries disappear entirely below a threshold level of PAR-3 (cyan curve in Figure 5E).

To distinguish these possibilities we used RNAi against PAR-3 to systematically vary the total abundance of PAR-3 in the system. We used a strain expressing endogenously tagged GFP:: PAR-3, allowing us to measure, for each embryo, the total density of membrane associated PAR-3, the mean oligomer size, and the asymmetry in PAR-3 in late maintenance phase. We focused our analysis on embryos that established PAR-3 and we verified that loss of asymmetry during maintenance was not caused by redistribution of PAR-3 by cortical flow (Figure S4). We confirmed the predicted dependence of mean oligomer size on total density of membrane-bound PAR-3 (Figure 5D). More importantly, plotting the observed PAR-3 asymmetry against mean oligomer size shows that the response to progressive depletion of PAR-3 strongly resembles, both qualitatively and quantitatively, the response predicted for the positive feedback scenario. We conclude that asymmetric recruitment of PAR-3 to the cell membrane results from positive feedback, and that this positive feedback on recruitment, combined with positive feedback due to

size dependent dissociation of PAR-3 oligomers, is sufficient to support stable PAR-3 asymmetries during maintenance in embryos lacking posterior inhibition by PAR-1.

Our finding that asymmetric recruitment of PAR-3 does not require an intact CR1 domain suggests that positive feedback on recruitment acts one or more intermediates. We therefore looked for molecules that are known to be asymmetrically enriched in maintenance phase zygotes and which are required for asymmetric recruitment of PAR-3(ΔCRT1)::GFP and to maintain PAR-3 asymmetry in *par-1* mutant embryos. This search identified the anterior polarity proteins CDC-42, PAR-6 and PKC-3. In *par-1* heterozygote embryos depleted of CDC-42 (*par-1/+;cdc-42(RNAi)*) , PAR-3::GFP asymmetries formed during polarity establishment phase and persisted through maintenance phase, relaxing towards lower levels as observed in controls (Figure 6A,B). The overall PAR-3 density and mean oligomer size were higher in these embryos than in undepleted controls (Figure 6A,B). However, despite the increased asymmetry in the localization of PAR-3, asymmetric recruitment of PAR-3(ΔCR1)::GFP was strongly reduced in *par-1/+;cdc-42(RNAi)* embryos during maintenance phase. In *par-1* homozygotes depleted of CDC-42 (*par-1/par-1;cdc-42(RNAi))*, PAR-3:GFP again became enriched during polarity establishment phase to higher levels than observed in untreated homozygous controls, but these asymmetries were almost completely lost during polarity maintenance phase (Figure 6A,D). This loss of asymmetry was not due to destabilization of PAR-3 oligomers because the rate constant for dissociation of PAR-3 from oligomers is unaffected by depletion of CDC-42 (Figure 6F). Thus CDC-42 is required for asymmetric recruitment of PAR-3 monomers to the plasma membrane under conditions where PAR-3 itself remains asymmetrically enriched, and it is required to maintain PAR-3 asymmetries in embryos lacking posterior inhibition by PAR-1.

Previous studies have shown that expanding CDC-42 activity towards the posterior pole by depleting its posterior inhibitor CHIN-1 [16,22,24] has no effect on asymmetric enrichment of PAR-3 during maintenance phase [16]. Here we found that depletion of CHIN-1 has no effect on asymmetric recruitment of PAR-3(ΔCR1)::GFP during maintenance phase (Figure 6E). Thus the role of CDC-42 in promoting asymmetric recruitment of PAR-3 does not appear to require its asymmetric activation.

Because CDC-42 regulates polarity through its ability to recruit and activate PAR-6 and PKC-3 [17,44,45], we asked whether these proteins are also involved in stabilizing PAR-3 asymmetries during maintenance phase. Because PAR-6 and PKC-3 function as a heterodimer, we focused on depletion of PAR-6. Consistent with previous reports [17,46,47], in control (*par-1* heterozygote) embryos depleted of PAR-6, cortical flows and segregation of PAR-3 were reduced during polarity establishment phase, but cortical asymmetries still form. During maintenance phase, a rapid decrease in cluster size and density, and redistribution of PAR-3 clusters by posterior directed flows, accompanied a complete loss of PAR-3 asymmetry. The disappearance of PAR-3 clusters was not due to inhibition by PAR-1 [12], because depletion of PAR-6 in *par-1* homozygous mutant embryos produced similarly rapid and complete loss of PAR-3 clusters during maintenance phase. Blocking the posterior-directed flows by co-depletion of MRCK-1 [16] and PAR-6 did not prevent the complete loss of PAR-3 asymmetry in *par-1* heterozygote embryos. However, the loss of asymmetry was reduced in par-1 homozygotes co-depleted of PAR-6 and MRCK-1 relative to those depleted of PAR-6 alone, albeit to a lesser extent. Thus PAR-6 (and presumably PKC-3) helps to reinforce PAR-3 asymmetries in the absence of PAR-1.

Using single molecule imaging at low duty ratios, we confirmed that the rapid decrease in PAR-3 oligomer number and intensity in *par-6(RNAi)* embryos was not due to increased rates of monomer dissociation from PAR-3 oligomers (Figure 6F, Figure S5). This suggests that the loss of PAR-3 asymmetry could be due to weaker feedback on PAR-3 recruitment. Consistent with this possibility, asymmetric recruitment of PAR-3(ΔCR1)::GFP was strongly reduced in *par-6(RNAi)* embryos, relative to controls, during early maintenance phase when PAR-3 remains asymmetric (Figure 6A,B,E). Asymmetric recruitment of PAR-3(ΔCR1)::GFP was completely abolished in late maintenance phase in *par-6(RNAi)* or *par-6(RNAi); mrck-1(RNAi) embryos* (Figure 6E). Because PAR-3 asymmetries are lost at this stage these results do not imply that PAR-6 is required for positive feedback on PAR-3 recruitment. However, they do provide further evidence against the existence of a cryptic driver of asymmetric recruitment that does not depend on PAR-3 (or other aPAR) asymmetry. Altogether these results suggest that CDC-42, PAR-6 and PKC-3 make essential contributions to stabilizing PAR-3 asymmetries in the absence of inhibition by PAR-1 and that they do so by supporting a positive feedback loop in which asymmetrically enriched PAR-3 promotes asymmetric binding of PAR-3 to the membrane.

Materials and Methods

C. elegans culture and RNAi

We cultured *C. elegans* strains under standard conditions [48] on 60mm petri plates containing E. coli bacteria (OP50) raised on normal growth medium (NGM). Table 1 provides a list of strains used in this study. Unless otherwise specified, strains were provided by the Caenorhabditis Genetics Center, which is funded by the National Center for Research Resources.

We performed RNAi experiments using the feeding method [49]. Bacteria targeting *par-1*, *par-3*, *par-6*, *cdc-42*, *mrck-1*, *spd-5*, and *nmy-2* were obtained from the from the Kamath RNAi library [50]. Bacteria targeting GFP and *perm-1* were obtained from Jeremy Nance and Karen Oegema respectively. Briefly, we grew bacteria to log phase in LB with 50µg/ml ampicillin, seeded ~300µl of culture onto NGM plates supplemented with 50µg/ml ampicillin and 1mM IPTG, incubated plates at room temperature for two days, and then stored them at 4˚C for up to one week before use. We transferred L4 larvae or you8ng adults (for *par-3(RNAi*)) to feeding plates and then cultured them at 25˚C for the following durations before imaging: (0 - 8 hours) for *par-3(RNAi*): 12-16 hours for *perm-1(RNAi*), and >24 hours for all others. We verified strong depletions of PAR-6 and CDC-42 by observing symmetric first cleavages, strong depletions of NMY-2 and MRCK-1 by observing absence of cortical flows during polarity establishment and/or maintenance phases.

Live imaging

For single molecule imaging experiments, we mounted embryos in egg salts containing ~21 μm diameter polystyrene beads. For all other experiments, we mounted embryos in eggs salts on agarose pads.

For data collected in Figures 3, 5, and 6E, we used an Olympus IX50 inverted microscope equipped with an Olympus OMAC two-color TIRF illumination system, a CRISP autofocus module (Applied Scientific Instrumentation), and a 1.49 NA oil immersion TIRF objective. Laser illumination at 488 nm from a 50-mW solid-state Sapphire laser (Coherent) was delivered

by fiber optics to the TIRF illuminator. Images were magnified by 1.6x and collected on an Andor iXon3 897 EMCCD camera, yielding a pixel size of 100 nm. Image acquisition was controlled by Andor IQ software. For the data collected in Figures 2, 4, and 6A-D,F, we used a Nikon Ti2-E inverted microscope equipped with a LunF XL laser combiner housing solid state 488nm, 561nm and 640nm lasers and feeding three separate TIRF illumination arms, a Ti2 N-ND-P Perfect Focus unit. perfect focus unit, and a CFI APO 100X 1.49NA TIRF lens. Images were magnified by 1.5X and collected on an Andor IXON Life 897 EM-CCD camera to achieve a pixel size of ~106nm. Image acquisition was controlled by Nikon Elements software.

For all experiments, we set the laser illumination angle to standard values that we chose empirically to approximately maximize signal-to-noise ratio while maintaining approximately even illumination across the field of view. All embryos were oriented with their AP axis perpendicular to the axis of TIRF illumination to avoid confounding effects of illumination gradients in comparisons of Anterior vs Posterior PAR dynamics. Further details of the imaging conditions used for specific quantitative analyses are provided below.

Image analysis

Particle detection and tracking were carried out as previously described [15,16]. Briefly, we use a slight modification of methods introduced by Crocker and Grier [51] to detect diffraction-limited features of interest as local intensity peaks in bandpass filtered images then determine their centroids and background-subtracted integrated intensities. We use µTrack software developed by Jaqaman and colleagues [52] to track features over time. Integration of particle detection and tracking and all subsequent analyses were carried out using custom scripts written in MATLAB and available upon request.

Timelapse analysis of PAR-3 oligomer dynamics

We measured PAR-3 oligomer dynamics in a *par-1* mutant strain expressing a C terminal fusion of PAR-3 from the endogenous locus. We collected images in timelapse mode using 10% laser power, 50msec exposure times at 3 sec intervals to minimize photobleaching. For each embryo and each timepoint, we identified PAR-3 clusters within anterior and posterior regions of interest (ROIs) and measured their background-subtracted intensities. We then determined the minimal polygon containing all detected particles and used its area to compute the densities of clusters or total PAR-3 fluorescence. For individual embryos, we plotted the smoothed mean intensities vs time to determine the timepoint in late establishment phase when mean intensities began to fall sharply, which coincided roughly with the onset of pseudocleavage (PC) furrow relaxation. Then we used this timepoint to align data across multiple embryos. We then computed means and standard errors across embryos from un-normalized data.

Measurements of PAR-3 oligomer size distribution

To measure the distribution of PAR-3 oligomer sizes in late maintenance phase, we first identified embryos in establishment phase before pseudocleavage. We used 30% laser power and 50msec exposures at 1 sec intervals to focus on the cortex while minimizing photobleaching. Following pseudocleavage relaxation, we waited for 4 minutes and then imaged PAR-3::GFP embryos using 100% laser power and a 50 μs exposure time in streaming acquisition for 50 seconds. For each embryo, we pooled all speckles detected in the first three frames and used these to estimate the distribution of PAR-3::GFP oligomer intensities. During the last 20 seconds of continuous exposure to 100% laser power, the distribution of speckle intensities approximated

a Gaussian distribution with a mean that roughly matched previous measurements of single molecule GFP intensities in near-TIRF imaging [15].

We used three different methods to estimate the distribution of PAR-3 oligomer sizes. The first method was based on Bayesian inference. We initially assumed that each particle had an equal prior probability of containing between 1 and 20 subunits. We then calculated the posterior probability each particle containing 1 to 20 subunits given the conditional probabilities of an oligomer of each size producing the observed fluorescence intensity, assuming means and variances for the distributions of n-mer intensities were equal to the mean and variance of the single molecular distribution multiplied by n. These posterior probabilities were used to update the prior probabilities and the process was repeated for 20 iterations, over which the prior and posterior probability distributions converged. We considered this converged distribution to be the steady-state distribution of oligomer sizes in maintenance phase.

The second method was a maximum likelihood estimate of the distribution of oligomer sizes. To do this, we assumed the distribution of particle intensities was equal to a weighted sum of the distributions of n-mers of size 1 to 20. The distributions of n-mer intensities were determined as described above. We determined the most likely values for each of the weights using the lsqnonlin function in MATLAB and considered these weights to constitute the steady-state distribution of oligomer sizes in maintenance phase.

The final method to determine the size distribution of PAR-3 oligomers was simply to bin particles by intensity based on the mean intensities of single molecules for each embryo. This very simple method produced roughly the same results as the other two, and therefore was used to produce the size distributions shown in Figure 3.

Measurements of single molecule dissociation rates

To measure single molecule dissociation rates, levels of transgenic PAR-3::GFP were reduced using RNAi against GFP [15]. Single PAR-3 molecules were imaged with 50 μs exposures to 100% laser power with various duty cycles. For each duty cycle, we performed single particle tracking and generated release curves from the resulting trajectories. We estimated the single molecule dissociation rate by fitting these release curves to single-term exponential decay functions. Fitting was performed for the regions of the curves where $t \geq 0.5$ seconds to exclude rapid exchange of PAR-3 monomers between the membrane and cytoplasm from the analysis. For each duty cycle, the measured exponential decay term is expected to be the sum of the dissociation rate of PAR-3 monomer from oligomers and the photobleaching rate, with in turn is expected to be proportional to the duty cycle [15]. To disentangle these two rates, we plotted the measured exponential decay term against duty cycle and fit a line to the data using linear regression. The slope of this fitted linear approximates the photobleaching rate, while the y-intercept approximates the true dissociation rate.

Measurements of oligomer size-dependent dissociation and short-term mobility rates

Oligomer size-dependent dissociation and diffusion rates were estimated from imaging data of NeonGreen::PAR-3 in streaming acquisition with 50 μs exposure times in maintenance phase of embryos depleted of NMY-2. Particle tracking was performed on the first 1 second of imaging to avoid confounding effects of photobleaching on oligomer size inference. The size of each tracked particle was inferred based on its intensity using the single molecule distribution as a standard. For each inferred oligomer size, the dissociation rate was inferred based on the

probability that oligomers disappear over a 50 μs interval and assuming a single-rate first-order dissociation reaction. The short-term mobility rate was calculated based on the frame-to-frame displacement over the same interval.

Measurements of PAR-3 binding asymmetries

To measure the relative binding rates of cytoplasmic PAR-3 molecules to the anterior and posterior membrane, we first photobleached PAR-3::GFP molecules by exposing embryos to 100% laser power in widefield for 5-10 seconds. We then imaged single PAR-3::GFP molecules in streaming acquisition in TIRF using 50 μs exposure time and 100% laser power. Crucially, we oriented all embryos perpendicular to the TIRF angle to avoid biases from non-uniform illumination. We performed single particle tracking as described above. We masked regions of the anterior and posterior cortex of approximately similar size by eye and measured the number of particle trajectories lasting at least 4 frames (0.2 seconds) that appeared within these masked regions. Finally, we divided the number of tracks by the number of pixels in the masked areas and used these normalized quantities to determine the ratio of anterior to posterior binding rates.

Mathematical modeling

For all simulations, we consider the following model of PAR-3 oligomerization and membrane binding (previously described in Lang and Munro 2022 [42]):

$$\frac{dP_1}{dt} = \left(k_{on}^{m} + k_f P_m\right)P_c - k_{off}^{m} P_1 - 2\left(k_{on}^{p} P_1 P_1 - k_{off}^{p} P_2\right) + \left(k_{on}^{c} P_c P_1 - k_{off}^{c} P_2\right)$$
$$- \sum_{i=3}^{N} \left(k_{on}^{p} P_1 P_{i-1} - k_{off}^{p} P_i\right)$$

$$\frac{dP_i}{dt} = k_{ass}\, P_{i-1} - (k_{ass} + k_{diss})P_i + k_{diss}P_{i+1} - \beta^{i-1}k_{off}^{m}P_N$$

$$\frac{dP_N}{dt} = k_{ass}\, P_{N-1} - k_{diss}P_N - \beta^{N-1}k_{off}^{m}P_N$$

$$P_{tot} = P_c + \sum_{i=1}^{N} iP_i$$

Where P_i is the concentration of PAR-3 particles with i subunits on the cell membrane, P_c is the concentration of cytoplasmic PAR-3 monomers, P_{tot} is the total amount of PAR-3 in the cell, which we assume is constant, k_{on}^{m} and k_{off}^{m} are the rates at which PAR-3 monomers exchange between the membrane and cytoplasm, k_{on}^{p} and k_{off}^{p} are the rates at which PAR-3 monomers exchange between the cell membrane and membrane-bound PAR-3 oligomers, k_{on}^{c} and k_{off}^{c} are the rates at which PAR-3 monomers exchange between the cytoplasm and membrane-bound PAR-3 oligomers, $k_{ass} = k_{on}^{p}P_1 + k_{on}^{c}P_c$, $k_{diss} = k_{off}^{p} + k_{off}^{c}$, k_f is a feedback-dependent rate at which cytoplasmic PAR-3 monomers bind the cell membrane, β is a constant between 0 and 1 that represents how membrane avidity increases with oligomer size, and N is the maximum oligomer size, which we set at 50.

We consider a scenario in which diffusion at the membrane is negligible and where the cytoplasm is well mixed. For simulations to assess polarity, we separate the membrane into two compartments that exchange components with a shared cytoplasm.

Simulations to determine how the ability to stabilize asymmetries depends on mean oligomer size and feedback strength.

To determine how the ability to stabilize asymmetries depends on mean oligomer size and feedback strength (defined as $\frac{k_f[PAR-3]}{k_{on}^m}$), we sampled parameter space as follows. k_{off}^p and k_{off}^m were set to 1 as the absolute values of these parameters does not affect the ability to stabilize an asymmetry. β was set to 0.25, as constrained by experimental measurements. All other parameters were randomly sampled with the constraints that $k_{on}^c \leq k_{on}^p$ [53], $k_f \leq 3k_{on}^m$, and $k_{off}^c = \frac{k_{on}^c k_{off}^p k_{off}^m}{k_{on}^m k_{on}^p}$ (which ensures that oligomerization dynamics satisfy detailed balance in the absence of feedback). After sampling, parameter sets were filtered such that the ratio of the fluxes of cytoplasmic monomers directly into clusters versus directly onto the membrane was no less than 0.1 and no greater than 2. Our previous modeling results show that more feedback is required to polarize as this ratio increases [42], and a simple analysis of fluxes in our model shows for measured values of $k_{off}^m \cong 3\ s^{-1}$ $k_{off}^c + k_{off}^p \cong 0.1\ s^{-1}$, this ratio cannot exceed 0.1. Therefore, the range of values sampled here provide is an extremely conservative estimate of this parameter. Polarization was assessed in a similar manner as previously described in Lang and Munro 2022 [42].

Simulations to determine how PAR-3 asymmetry depends on total PAR-3.

Initial parameters were chosen to reproduce the observed anterior-posterior asymmetry in PAR-3 concentration, anterior-posterior asymmetry in monomer recruitment, mean anterior oligomer size, and oligomer size-dependent dissociation rates. For simulations involving positive feedback, the asymmetry in recruitment rates was dependent on the feedback parameter k_f in the above equations. For simulations involving "asymmetric bias", constant anterior and posterior recruitment rates were selected to match the asymmetric recruitment produced in the simulation involving positive feedback. All other parameters were identical between these two cases. These two models produce identical steady state outcomes in initial simulations. Following the initial simulations, which correspond to a wild-type *C. elegans* embryo, simulations of progressive RNAi depletion were conducted where all parameters were kept constant except for the total PAR-3 (P_{tot}), which was iteratively decreased by 10% for 25 simulations. For each simulation, the steady state asymmetry was assessed.

Simulations to determine the timescale for relaxation of PAR-3 levels at the cell membrane to steady state.

To simulate the relaxation of PAR-3 levels at the membrane to steady state, we initially picked parameters that reproduced mean PAR-3 oligomer size and feedback strength observed in wild-type *C. elegans* embryos. We constrained k_{off}^{m} and k_{off}^{p} according to experimental measurements. We next increased k_{on}^{p} five-fold and ran simulations to allow PAR-3 levels to reach a steady state on the membrane. Finally, using this steady state as the initial simulation conditions, we reduced k_{on}^{p} five-fold and ran simulations for 250 seconds to mirror the timescale of maintenance phase in the *C. elegans* embryo.

To simulate the timescale for loss of an initial asymmetry in the absence of positive feedback, we initially picked parameters that reproduced mean PAR-3 oligomer size observed in wild-type *C. elegans* embryos and set the feedback parameter $k_f = 0$. We constrained k_{off}^m and k_{off}^p according to experimental measurements. We then increased k_{on}^p three-fold and ran a simulation with one membrane compartment to steady state. We then performed simulations where two membrane compartments exchange PAR-3 monomers with a shared cytoplasmic pool. For initial conditions, we used the steady state distribution of PAR-3 from the previous simulation for one compartment and set PAR-3 levels to zero for the other. We then reduced k_{on}^p three-fold and ran simulations for 250 seconds to mirror the timescale of maintenance phase in the *C. elegans* embryo.

PAR-3 depletion experiments

PAR-3 depletion experiments were carried out by growing worms on RNAi feeding plates for 2-8 hours. To qualitatively assess whether PAR-3 polarity was established prior to the onset of maintenance phase and whether posterior-directed cortical flows redistribute PAR-3 oligomers during maintenance phase, embryos were imaged using 30% laser power at 2.5-5 second intervals for 4 minutes following pseudocleavage relaxation. Immediately following this period, embryos were imaged in late maintenance phase using streaming acquisition with 100% laser power and 50 μs exposure for 50 seconds. Particle detection and particle size inference were performed as described above. We determined the fluorescence density of segmented PAR-3 particles in bins spanning 10-40% (anterior) and 60-90% (posterior) embryo length and calculated the anterior-posterior asymmetry of PAR-3 as the ratio of these values.

FRAP experiments

FRAP experiments were carried with the following protocol: images were collected with 50 μs exposures at 1 second intervals using 30% laser power in TIRF. Embryos were then exposed to 100% laser power in TIRF for 1.5 seconds to photobleach molecules at the cell surface. Recovery was then tracked by taking 50 μs exposures at 3 second intervals using 30% laser power.

Lang et al, Figure 1

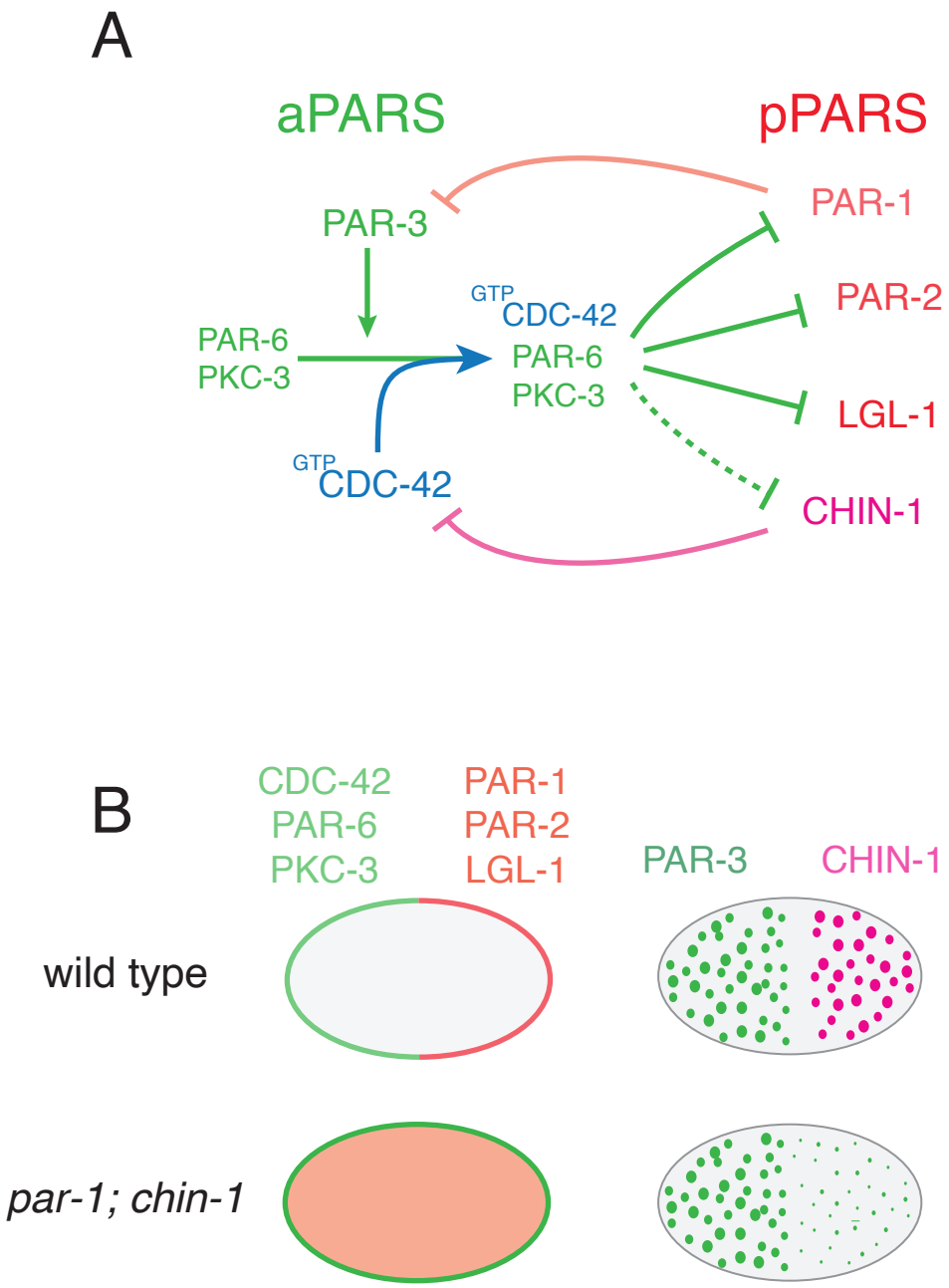

Figure 1. PAR polarity in the *C. elegans* embryo. (A) Schematic illustrating key interactions that maintain PAR asymmetries in the *C. elegans* zygote. On the left, PAR-3 promotes entry of the PAR-6/PKC-3 dimer into an active complex with active CDC-42. PKC-3 inhibits cortical accumulation of posterior PARs. PAR-1 inhibits cortical accumulation of PAR-3, while CHIN-1 inhibits CDC-042 activity. **(B)** In embryos lacking posterior inhibitors PAR-1 and CHIN-1, CDC-42, PAR-6 and PKC-3 are uniformly distributed at the membrane, all posterior PARs are absent or uniformly cytoplasmic, but PAR-3 oligomers remain asymmetrically distributed.

Lang et al, Figure 2

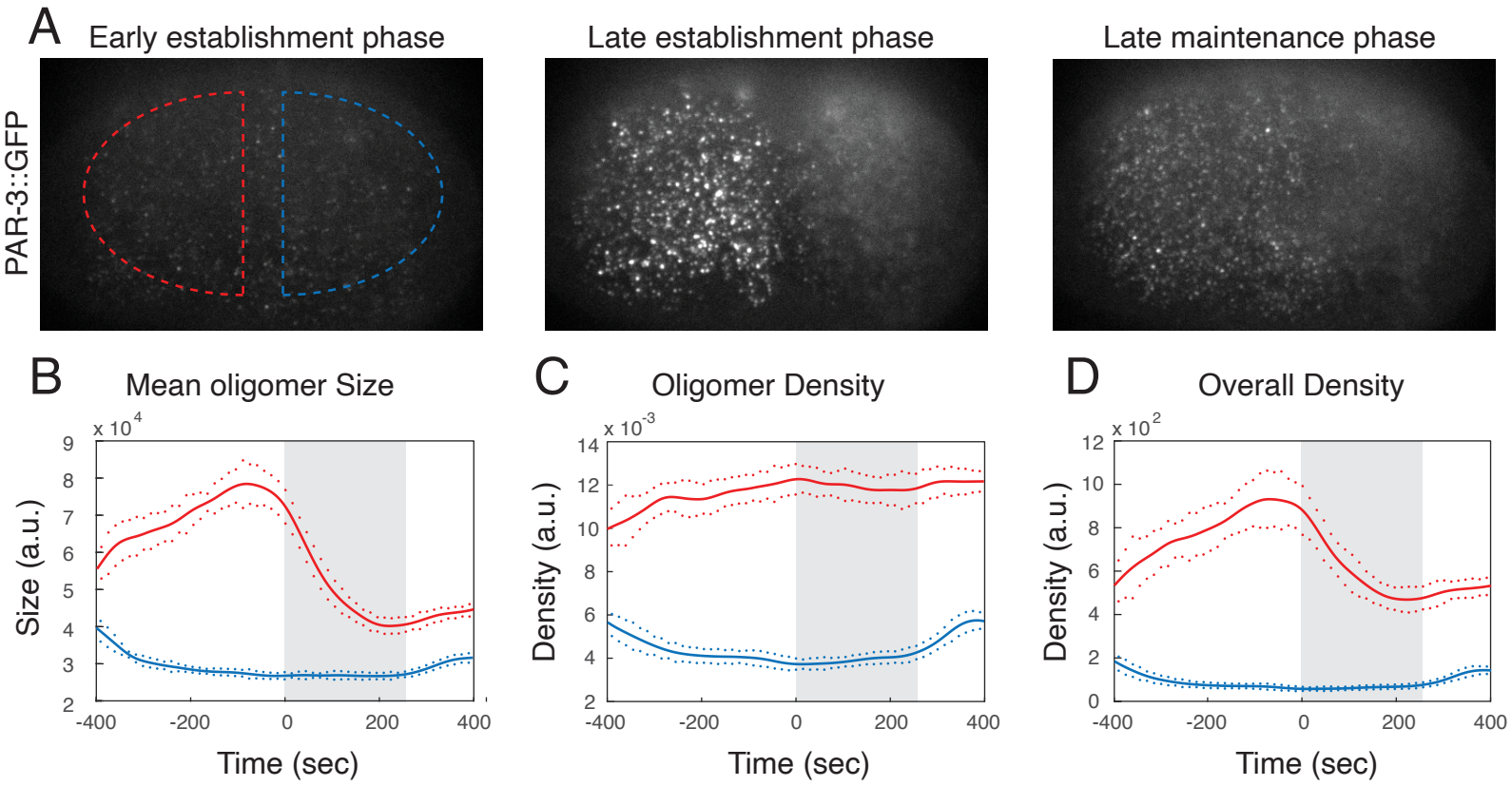

Figure 2. PAR-3 asymmetries are dynamically stable through mitosis. (A) Individual near-TIRF images from a time-lapse sequence showing PAR-3 oligomer intensities and distributions at the cell surface in homozygous *par-1* mutant embryos at early establishment, late establishment and late maintenance phase. **(B-D)** Results of particle tracking analysis showing **(B)** mean oligomer size, **(C)** oligomer density, and **(D)** total PAR-3 fluorescence density over time on the anterior (red) and posterior (blue) cortex in homozygous *par-1* mutant embryos. Data are from n = 12 embryos aligned with respect to the onset of maintenance phase. The grey shaded area indicates maintenance phase. Solid lines indicate the mean and dots indicate S.E.M. at each time point.

Lang et al, Figure 3

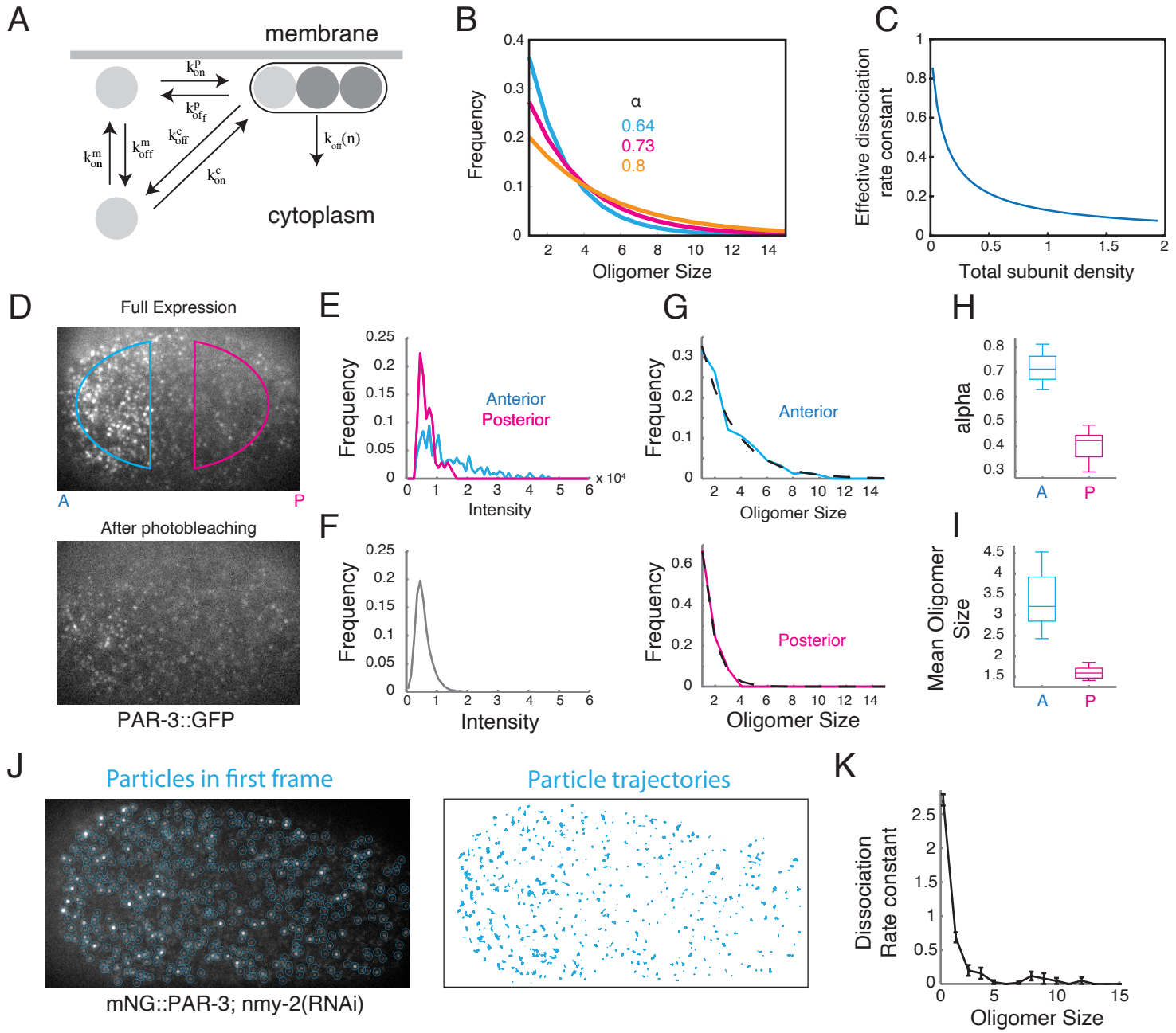

Figure 3. Size distributions and size-dependent dissociation of PAR-3 oligomers. (A) Schematic illustrating a simple model for PAR-3 oligomerization dynamics. Monomers bind and unbind the membrane with rate constants k_{on}^{m} and k_{off}^{m} respectively. Membrane-bound and cytoplasmic monomers bind oligomers on the membrane with rate constants k_{on}^{p} and k_{on}^{c} respectively, and subunits dissociate from oligomers to the membrane and cytoplasm with rate constants k_{off}^{p} and k_{off}^{c} respectively. Oligomers dissociate from the membrane according to a size-dependent rate constant $k_{off}(n)$ where n is the number of subunits in the oligomer. **(B)** When $k_{off}(n) = 0$ for $n > 1$, the model predicts that the steady state distribution of oligomer sizes is given by $P_i = P_1\alpha^{i-1}$ where P_i is the frequency of oligomers of size i and α represents oligomerization strength (see text for details) **(C)** Predicted dependence of the effective rate constant for PAR-3 dissociation ($k_{eff}^{diss} = \frac{\sum k_{off}(n)}{\sum nP_n}$), on total density of membrane-bound PAR-3, for the ideal scenario in which $k_{off}(n) = 0$ for $n > 1$. **(D)** PAR-3 speckle intensities before and after photobleaching in late maintenance phase *par-1* mutant embryos. Micrographs show near-TIRF images of PAR-3::GFP at the start of imaging (top panel) and after 30 seconds of continuous laser exposure at full power (bottom panel). **(E)** Representative examples of anterior (cyan) and posterior (magenta) speckle intensity distributions. **(F)** Representative example of speckle intensities after photobleaching (gray). **(G)** Inferred distributions of PAR-3 oligomer sizes on the anterior and posterior cortex of a representative embryo, based on calibrating raw intensities to the estimated intensity distribution of single molecules. Dashed lines indicate a fit of the equation $P_i = P_1\alpha^{i-1}$. Estimates of **(H)** mean oligomer size s and **(I)** oligomerization strength α on the anterior and posterior of n = 8 individual embryos in late maintenance phase (n=8). **(J)** (left) Representative micrograph of a maintenance phase embryo expressing mNG::PAR-3 and depleted of Myosin II heavy chain NMY-2 by RNAi. Blue circles indicate

detected PAR-3 speckles that were subsequently tracked to estimate dissociation rates. (Right) Plots of the trajectories for each of the individual speckles. Note that the individual trajectories are well-separated. **(K)** Estimated rate constants for dissociation rates of PAR-3 oligomers from the membrane as a function of inferred number of subunits. Error bars represent the S.E.M. Data were compiled from n = 3 individual embryos.

Lang et al, Figure 4

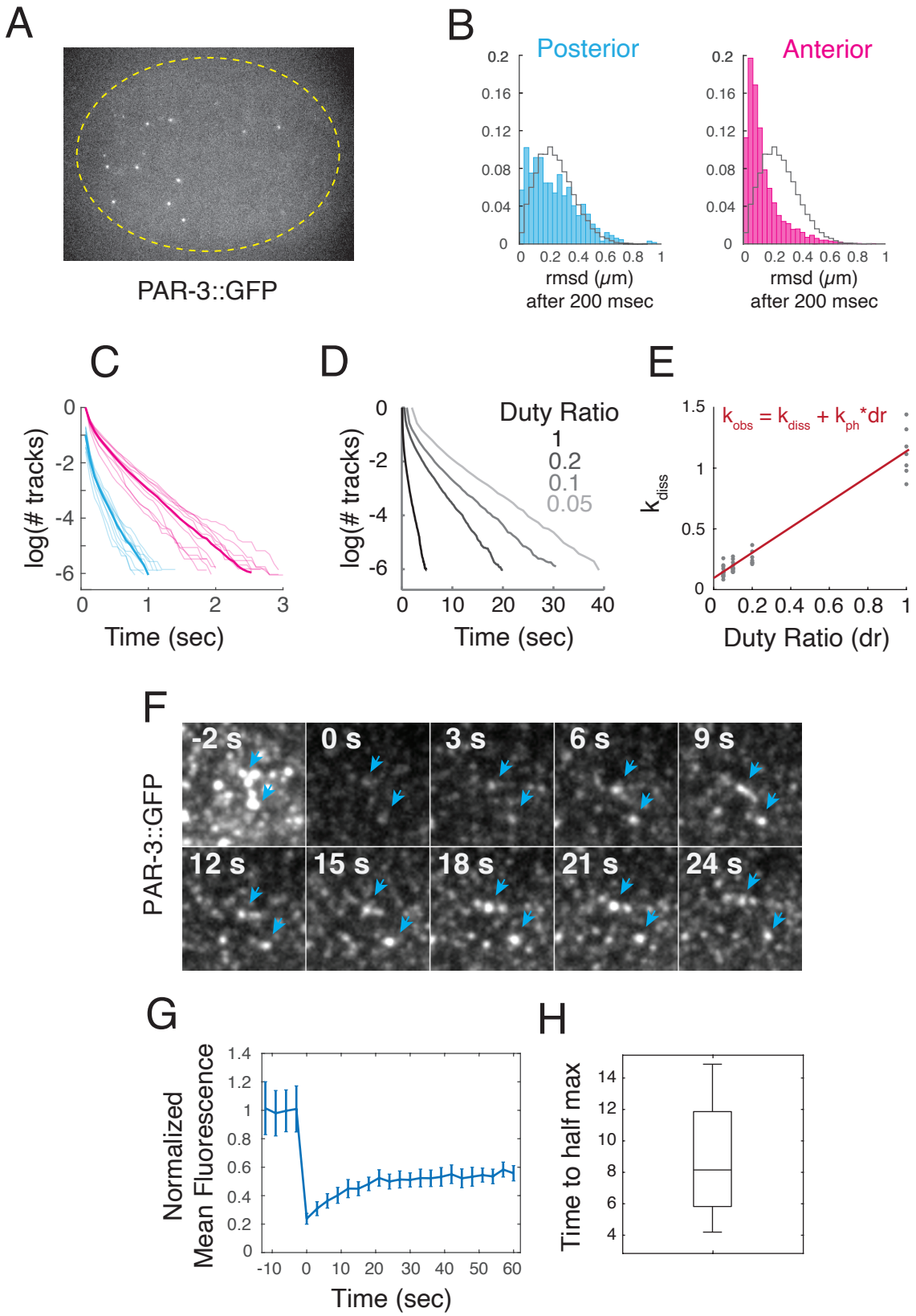

Figure 4.

(A) Representative image showing single molecules of PAR-3::GFP imaged at high laser power and short exposure times to allow accurate tracking of fast diffusing molecules. **(B)** Distributions of root mean square displacements after t = 200 msec ($RMSD_{200}$) measured for molecules tracked on the anterior and posterior cortex in n = 8 embryos. Red curve indicates simulated $RMSD_{200}$ distributions for molecules undergoing Brownian diffusion with diffusivity = 0.1 μm^2/sec. **(C)** Release curves measured for single molecules of PAR-3::GFP on the anterior and posterior cortex of wild type embryos under continuous illumination. Thin traces show release curves for individual embryos (n = 8); Thick traces show data summed for all embryos. Data were normalized by total numbers of anterior tracks. **(D)** Release curves for PAR-3::GFP molecules imaged with fixed laser power and exposure times but with different duty ratios (dr). Each curve represents the sum of data from multiple embryos: (dr = 1, n = 7; dr = 0.2; n = 7, dr = 0.1; n = 12; dr = 0.05, n = 13). **(E)** Plot of disappearance rate constants (k_{obs}) measured for different duty ratios (dr) by fitting the linear portions of the release curves (see Methods for details). The dashed line represents a linear least squares fit of the data to the equation $k_{obs} = k_{diss} + k_{pb} * dr$. The slope of the fit yields an estimate of the photobleaching rate k_{pb} = 1.04/sec and the y-intercept yields an estimate of the dissociation rate k_{diss}= 0.08/sec. **(F)** Representative micrographs showing the time course of recovery of PAR-3::GFP on the anterior cortex after photobleaching the entire cortex of the embryo in early maintenance phase. Timestamps indicate seconds after photobleaching. Blue arrowheads indicate individual PAR-3 oligomers that persist during recovery. **(G)** Plots of average fluorescence density vs time after photobleaching, corrected for the overall decrease in fluorescence observed during maintenance

phase. Error bars indicate SEM (n = 4 embryos) **(H)** Box plot indicating the time to reach half of maximum recovery for the data in **(G)**, n = 4 embryos).

Lang et al, Figure 5

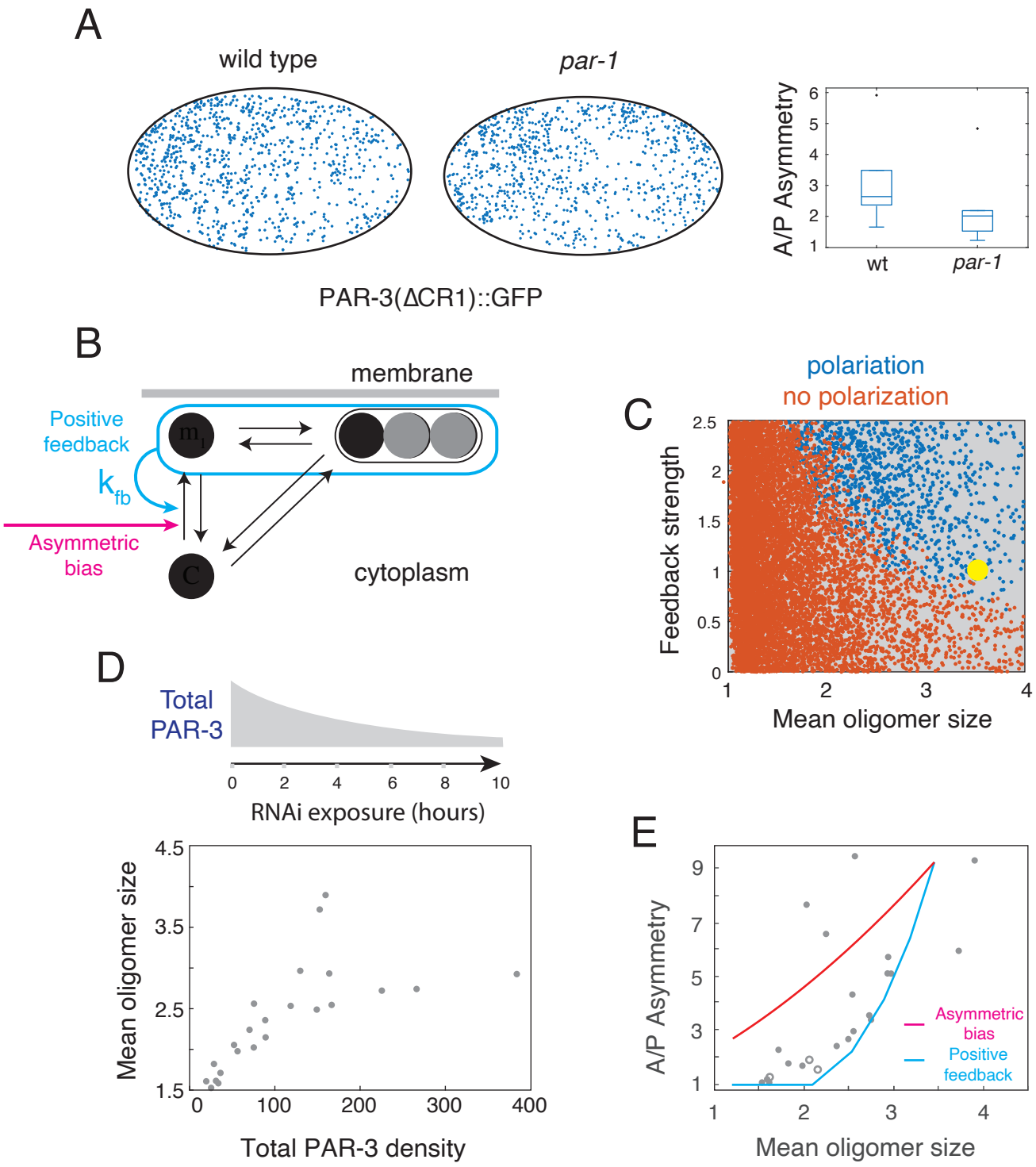

Figure 5. Positive feedback on membrane recruitment of PAR-3, plus feedback due to size-dependent dissociation of oligomers, are sufficient to stabilize PAR-3 asymmetries. (A) Spatial asymmetry of membrane binding events for oligomerization-defective PAR-3 molecules, measured during maintenance phase. Scatter plots on the left are representative distribution of binding events over space in control and *par-1* mutants, detected by single molecule imaging. Boxplots show the ratio of binding events in the anterior to posterior of the embryo (control: n = 5; *par-1*: n = 6). **(B)** Modified versions of the reaction diagram in Figure 3A, with alternative assumptions for the mechanism that underlies asymmetric recruitment: (cyan): Membrane-bound PAR-3 feeds back to promote recruitment of PAR-3 monomers to the membrane. (magenta): A fixed asymmetric input (whose strength is independent of PAR-3 densities) biases recruitment to the anterior cortex. **(B)** Phase plane derived for the version of the model with positive feedback on membrane recruitment, showing how the ability to polarize depends on mean oligomer size and feedback strength, defined as the ratio of feedback-dependent flux to basal flux onto the membrane. Experimental measurements of mean oligomer size and feedback strength in the *C. elegans* zygote place PAR-3 in the region of phase where space polarization is possible (yellow dot). **(C)** Schematic illustrating the PAR-3 depletion experiment. Top: concentration can be continuously tuned by varying feeding time on RNAi plates. (Bottom) Scatter plot showing the relationship between mean oligomer size and total membrane-bound PAR-3 across various levels of PAR-3 RNAi depletion. **(E)** Scatter plot showing the relationship between mean oligomer size and PAR-3 asymmetry during late maintenance phase. Filled dots represent embryos where polarity was established by late interphase and unfilled dots represent embryos where polarity was not established. The magenta line represents the predicted

relationship for the model in which asymmetric recruitment is the result of a cryptic bias and the cyan line represents the prediction of a model where it is the result of positive feedback.

Lang et al, Figure 6

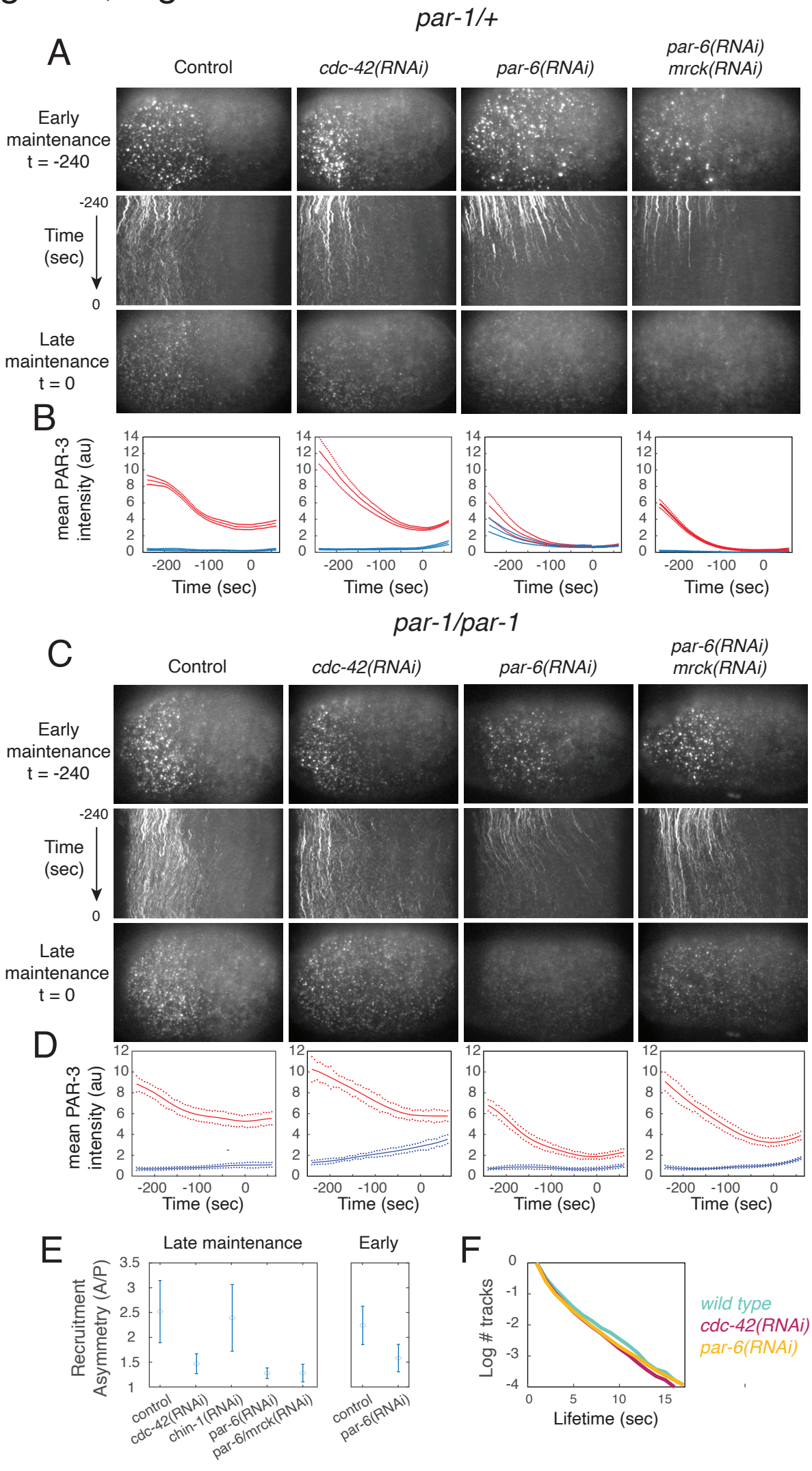

Figure 6. CDC-42 and PAR-6/PKC-3 reinforce PAR-3 asymmetries during maintenance phase by promoting asymmetric recruitment of PAR-3 (A) Representative micrographs showing PAR-3 oligomer sizes and distribution during maintenance phase in *par-1* heterozygote (*par-1/+*) embryos for the indicated RNAi depletions. Top and bottom micrographs show the distribution of PAR-3 oligomers at early (-240 sec) and late (0 sec) maintenance. Time is measured relative to the point where anterior density of PAR-3 reached a minimum in late maintenance phase (see Methods for details). Kymographs show how the distribution changes over the 240 seconds between these time points. Diagonal streaks in the kymographs indicate transport of PAR-3 oligomers by cortical flow. **(B)** Corresponding plots of total fluorescence density of PAR-3 within segmented speckles during maintenance phase. Bold lines indicate the mean and red dots indicate the standard error of the mean across individual embryos (control: n = 8, *cdc-42(RNAi)*: n = 7, *par-6(RNAi):* n = 6, *par-6(RNAi)*; *mrck-1(RNAi*): n = 8). **(C)** Representative micrographs showing PAR-3 oligomer sizes and distribution during maintenance phase in *par-1* homozygous (*par-1/par-1*) embryos for the indicated RNAi depletions. Data are presented as described in **(A)**. **(D)** Corresponding plots of total fluorescence density of PAR-3 within segmented speckles during maintenance phase. Bold lines indicate the mean and red dots indicate the standard error of the mean across individual embryos (control: n = 10, *cdc-42(RNAi)*: n = 6, *par-6(RNAi):* n = 9, *par-6(RNAi)*; *mrck-1(RNAi*): n = 14). **(E)** A:P ratio of rates (#/unit area) for binding of oligomerization-defective PAR-3 molecules to the cell membrane in wild type embryos expressing unlabeled wild-type PAR-3 and subjected to the indicated treatments. Error bars show the S.E.M. (control early: n = 5, control late: n = 6, *cdc-42(RNAi)*: n = 6, *chin-1(RNAi)*: n = 8, *par-6(RNAi) early:* n = 7, *par-6(RNAi) late:* n = 7, *par-6(RNAi)*; *mrck-1(RNAi*): n = 6). **(F)** Release curves for single molecules of transgenic PAR-3::GFP measured in

control, *cdc-42(RNAi)* and *par-6(RNAi)* embryos during maintenance phase using high laser power, short exposures and low duty ratios to achieve accurate tracking with low photobleaching. All data were collected under identical conditions. Each curve represents the average over (control: n = 8), (*cdc-42(RNAi)*: n = 12) and (*par-6(RNAi)*: n = 14) embryos. See Figure S5 for the individual release curves.

Lang et al, Figure S1

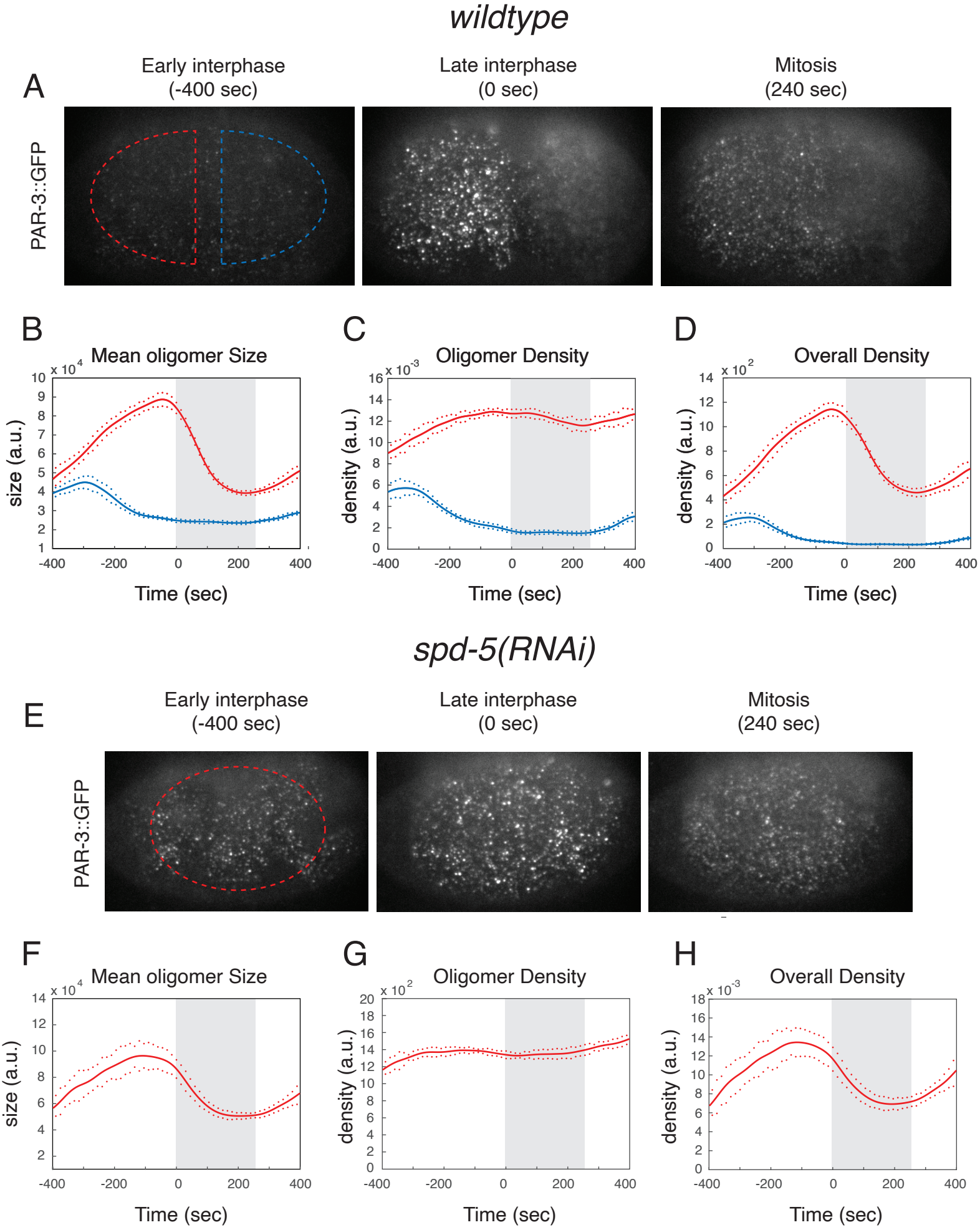

Supplementary Figure 1 (related to Figure 2) PAR-3 oligomer dynamics during maintenance phase in wild type and *spd-5(RNAi)* embryos) (A) Individual near-TIRF images from a time-lapse sequence showing PAR-3 oligomer intensities and distributions at the cell surface in control (*par-1* heterozygote) embryos at early establishment, late establishment and late maintenance phase. **(B-D)** Results of particle tracking analysis showing **(B)** mean oligomer size, **(C)** oligomer density, and **(D)** total PAR-3 fluorescence density over time on the anterior (red) and posterior (blue) cortex in control embryos. Data are from n = 8 embryos aligned with respect to the onset of maintenance phase. The grey shaded area indicates maintenance phase. Solid lines indicate the mean and dots indicate S.E.M. at each time point. **(E)** Individual near-TIRF images from a time-lapse sequence showing PAR-3 oligomer intensities and distributions at the cell surface in *spd-5(RNAi)* embryos at early establishment, late establishment, and late maintenance phase. **(F-H)** Results of particle tracking analysis showing **(F)** mean oligomer size, **(G)** oligomer density, and **(H)** total PAR-3 fluorescence density over time on the cortex. Data are from n = 6 embryos aligned with respect to the onset of maintenance phase. The grey shaded area indicates maintenance phase. Solid lines indicate the mean and dots indicate S.E.M. at each time point.

Lang et al, Figure S2

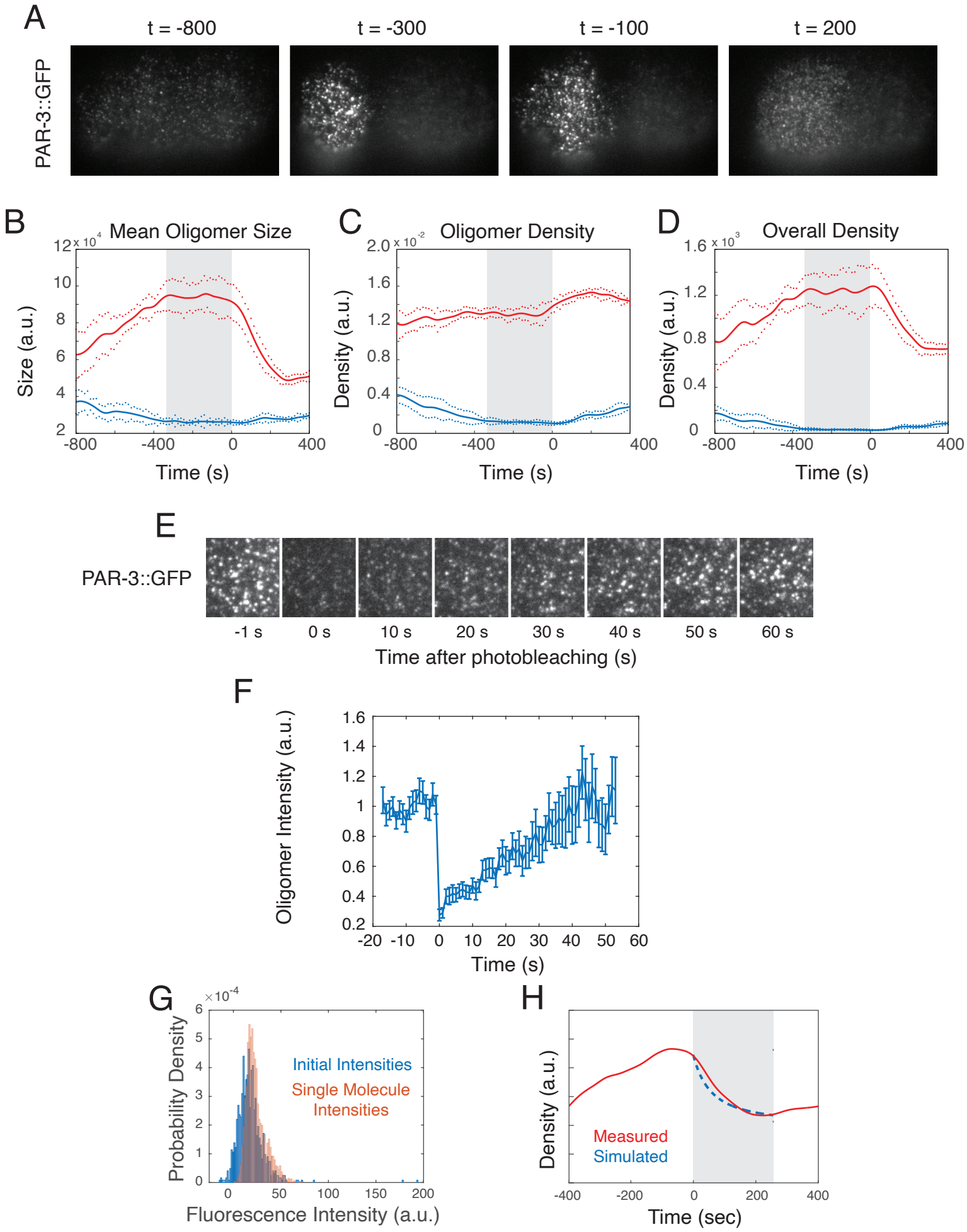

Supplementary Figure 2 (related to Figure 3 and 4) Dynamic exchange of subunits with PAR-3 oligomers. (A) Individual near-TIRF images from a time-lapse sequence showing PAR-3 oligomer intensities and distributions at the cell surface in *pri-1(RNAi*) embryos at early establishment (t = -800), two time points (t = -300 and t = -100) during extended late establishment and late maintenance (t = 200) phase. **(B-D)** Results of particle tracking analysis showing **(B)** mean oligomer size, **(C)** oligomer density, and **(D)** total PAR-3 fluorescence density over time on the anterior (red) and posterior (blue) cortex in *pri-1(RNAi*) embryos. Data are from n = 6 embryos aligned with respect to the onset of maintenance phase. The grey shaded area indicates extended late establishment phase in which the mean oligomer size and overall density of PAR-3 remain ~ constant. Solid lines indicate the mean and dots indicate S.E.M. at each time point. **(E)** Representative micrographs showing the time course of recovery of PAR-3::GFP on the anterior cortex after photobleaching the entire cortex of the embryo during late establishment phase in a *pri-1(RNAi*) embryo. Timestamps indicate seconds after photobleaching. **(F)** Plots of average fluorescence density vs time after photobleaching for n = 22 individual clusters that could be tracked over an 80 second interval before, during and after photobleaching. Error bars indicate SEM (n = 22 clusters in 4 embryos) **(G)** Overlay of the distributions of background-subtracted intensities of (blue) newly detected PAR-3::GFP speckles and (red) single molecules speckles after photobleaching in the same cells. These measurements were made on the same data (Figure 3J) used to estimate size-dependent oligomer dissociation. (H) (red) measured time course of decrease in total PAR-3::GFP fluorescence associated with segmented speckles during maintenance phase. (blue) the time course predicted by simulations assuming linear oligomers and using the measured values for mean oligomer size in late

maintenance and rate constants for size-dependent dissociation of monomers and oligomers from the membrane, and monomers from membrane-bound oligomers.

Lang et al, Figure S3

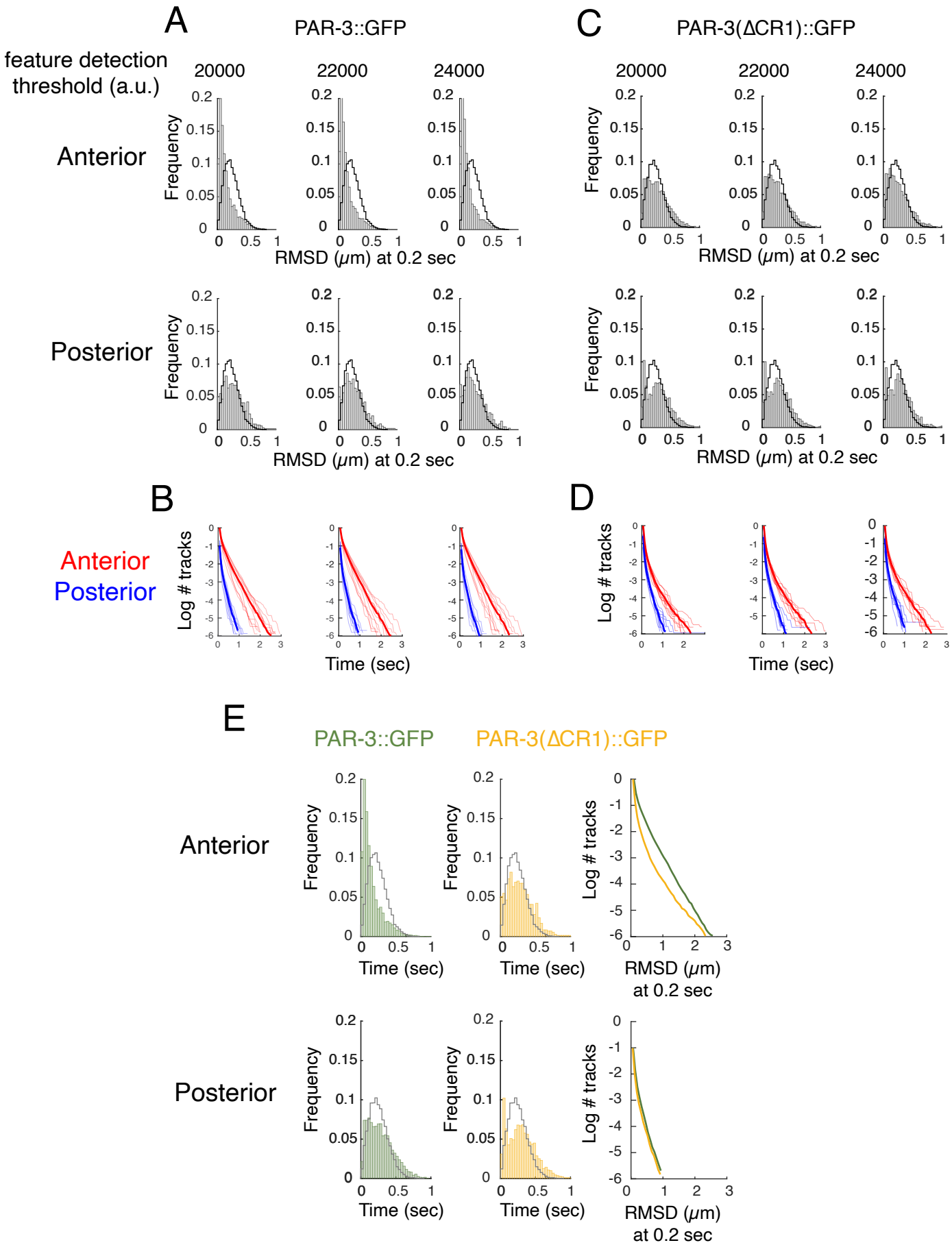

Supplementary Figure 3 (related to Figure 4 and 6). Single molecule measurements of PAR-3::GFP and PAR-3(CR1)::GFP. (A-B) Plots of RMSD distributions and release curves for single molecules of PAR-3::GFP in *par-1* heterozygotes. **(A)** Distributions of root mean square displacements after t = 200 msec ($RMSD_{200}$) measured for molecules tracked on the anterior and posterior cortex in n = 8 embryos. Each column represents data obtained using a different integrated intensity threshold for detecting single molecules, as indicated by the value for feasturre detection threshold. Dark curve indicates simulated $RMSD_{200}$ distributions for molecules undergoing Brownian diffusion with diffusivity = 0.1 μm^2/sec. **(B)** Release curves measured for single molecules of PAR-3::GFP on the anterior and posterior cortex of wild type embryos under continuous illumination fort different feature detection thresholds. Thin traces show release curves for individual embryos (n = 8); Thick traces show data summed for all embryos. Data were normalized by total numbers of anterior tracks. **(C-D)** Plots of RMSD distributions and release curves for single molecules of PAR-3(ΔCR1)::GFP in *par-1* heterozygotes. **(B)** Distributions of root mean square displacements after t = 200 msec ($RMSD_{200}$) measured for molecules tracked on the anterior and posterior cortex in n = 9 embryos. Each column represents data obtained using a different integrated intensity threshold for detecting single molecules, as indicated by the value for feasturre detection threshold. Dark curve indicates simulated $RMSD_{200}$ distributions for molecules undergoing Brownian diffusion with diffusivity = 0.1 μm^2/sec. **(D)** Release curves measured for single molecules of PAR-3::GFP on the anterior and posterior cortex of wild type embryos under continuous illumination fort different feature detection thresholds. Thin traces show release curves for individual embryos (n = 9); Thick traces show data summed for all embryos. Data were normalized by total numbers of anterior tracks. (E) Direct comparisons of anterior and posterior RMSD distributions and release curves for PAR-3::GFP and PAR-3(ΔCR1)::GFP. Data from (A-

D) with feature detection threshold = 20000 were used for the comparison. Only the mean release curves are shown on the right.

Lang et al, Figure S4

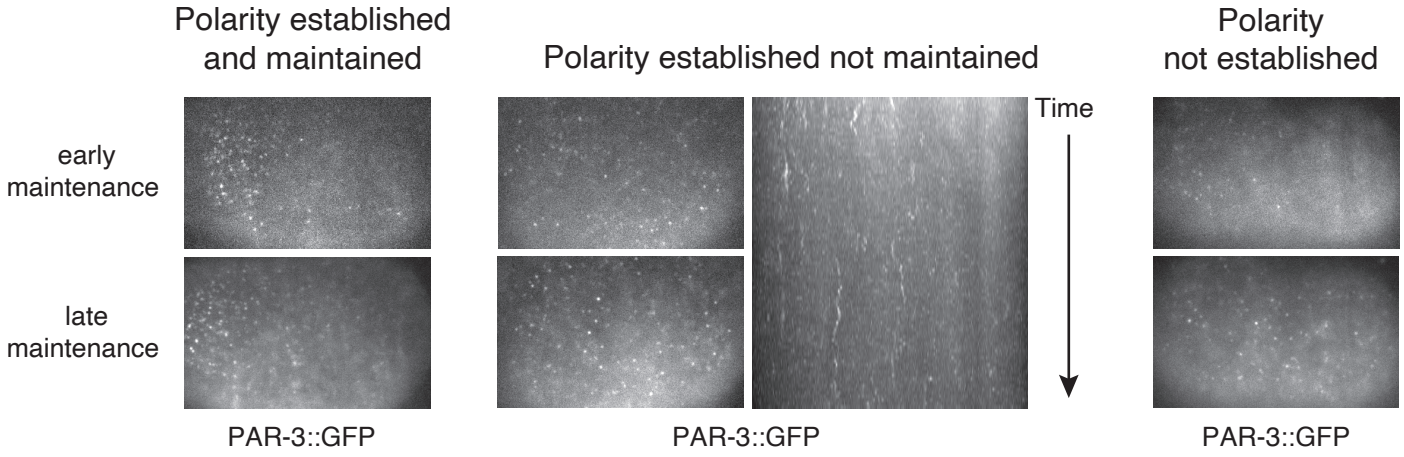

Supplementary Figure 4 (related to Figure 5). Examples of different phenotype classes in the PAR-3 depletion experiment shown in Figure 5D-E. Top and bottom micrographs show the distribution of PAR-3 at early and late maintenance respectively. We observed three distinct classes: (left) Polarity established and maintained, (middle) polarity established and not maintained and (right) Polarity never established. For the middle class, the kymograph confirms that the loss of PAR-3 asymmetry was not due to redistribution of PAR-3 by posterior-directed cortical flows.

Lang et al, Figure S5

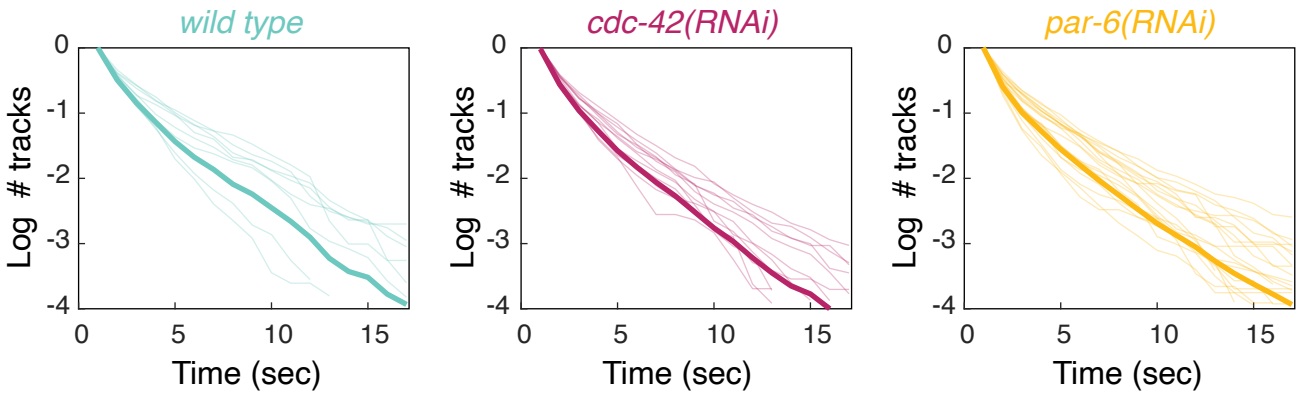

Supplementary Figure 5 (related to Figure 6). Individual release curves for single molecules of PAR-3::GFP in control, *cdc-42(RNAi)* and *par-6(RNAi)* embryos. Release curves for single molecules of transgenic PAR-3::GFP measured in control, *cdc-42(RNAi)* and *par-6(RNAi)* embryos during maintenance phase using high laser power, short exposures and low duty ratios to achieve accurate tracking with low photobleaching. All data were collected under identical conditions. Each thin curve represents data from a single embryo. Thick curves represent the average over (control: n = 8), (*cdc-42(RNAi)*: n = 12) and (*par-6(RNAi)*: n = 14) embryos.

Table 1. *C. elegans* strains used in this study.

Name	Genotype	Origin
Em267	par-3(it298[PAR-3::GFP]) III	Kenneth Kemphues
Em292	par-3(it298[PAR-3::GFP]) III; rol-4(sc8) par-1(it0051) V/DnT1 IV;V	Kenneth Kemphues
Em307	itIs268[ppar-3::PAR-3(V80D D198K)::GFP + unc-119(+)]; unc-119(ed3) III #5	Kenneth Kemphues
Em327	*par-6(cp60[par-6::mKate2::3xMyc + LoxP unc-119(+) LoxP]) I par-3(cp54[mNG::3xFlag::par-3]) III;*	Daniel Dickinson
Em297	par-3(it298[PAR-3::GFP]) III; NMY-2(ne3409) I	
Em241	mrck-1(ok586) V/nT1 [qIs51] (IV;V); ddIs??[pie-1::PAR6::GFP + unc119(+)]; itIs192[pie::GFP::PAR-3 unc119(+)]	

References

1. Goldstein, B., and Macara, I.G. (2007). The PAR proteins: fundamental players in animal cell polarization. Dev Cell *13*, 609–622. 10.1016/j.devcel.2007.10.007.

2. Lang, C.F., and Munro, E. (2017). The PAR proteins: from molecular circuits to dynamic self-stabilizing cell polarity. Development *144*, 3405–3416.

3. Cuenca, A.A., Schetter, A., Aceto, D., Kemphues, K., and Seydoux, G. (2003). Polarization of the C. elegans zygote proceeds via distinct establishment and maintenance phases. Development *130*, 1255–1265.

4. Bienkowska, D., and Cowan, C.R. (2012). Centrosomes can initiate a polarity axis from any position within one-cell C. elegans embryos. Curr Biol *22*, 583–589.

5. Cowan, C.R., and Hyman, A.A. (2004). Centrosomes direct cell polarity independently of microtubule assembly in C. elegans embryos. Nature *431*, 92–96.

6. Zhao, P., Teng, X., Tantirimudalige, S.N., Nishikawa, M., Wohland, T., Toyama, Y., and Motegi, F. (2019). Aurora-A Breaks Symmetry in Contractile Actomyosin Networks Independently of Its Role in Centrosome Maturation. Dev Cell *49*, 651–653. 10.1016/j.devcel.2019.05.010.

7. Klinkert, K., Levernier, N., Gross, P., Gentili, C., von Tobel, L., Pierron, M., Busso, C., Herrman, S., Grill, S.W., Kruse, K., et al. (2019). Aurora A depletion reveals centrosome-independent polarization mechanism in Caenorhabditis elegans. eLife *8*, e44552. 10.7554/eLife.44552.

8. Longhini, K.M., and Glotzer, M. (2022). Aurora A and cortical flows promote polarization and cytokinesis by inducing asymmetric ECT-2 accumulation. eLife *11*, e83992. 10.7554/eLife.83992.

9. Kapoor, S., and Kotak, S. (2019). Centrosome Aurora A regulates RhoGEF ECT-2 localisation and ensures a single PAR-2 polarity axis in C. elegans embryos. Development *146*, dev174565. 10.1242/dev.174565.

10. Cheeks, R.J., Canman, J.C., Gabriel, W.N., Meyer, N., Strome, S., and Goldstein, B. (2004). C. elegans PAR proteins function by mobilizing and stabilizing asymmetrically localized protein complexes. Curr Biol *14*, 851–862.

11. Munro, E., Nance, J., and Priess, J.R. (2004). Cortical flows powered by asymmetrical contraction transport PAR proteins to establish and maintain anterior-posterior polarity in the early C. elegans embryo. Dev Cell *7*, 413–424.

12. Motegi, F., Zonies, S., Hao, Y., Cuenca, A.A., Griffin, E., and Seydoux, G. (2011). Microtubules induce self-organization of polarized PAR domains in Caenorhabditis elegans zygotes. Nat Cell Biol *13*, 1361–1367.

13. Zonies, S., Motegi, F., Hao, Y., and Seydoux, G. (2010). Symmetry breaking and polarization of the C. elegans zygote by the polarity protein PAR-2. Development *137*, 1669–1677.

14. Goehring, N.W., Hoege, C., Grill, S.W., and Hyman, A.A. (2011). PAR proteins diffuse freely across the anterior-posterior boundary in polarized C. elegans embryos. J Cell Biol *193*, 583–594.

15. Robin, F.B., McFadden, W.M., Yao, B., and Munro, E.M. (2014). Single-molecule analysis of cell surface dynamics in Caenorhabditis elegans embryos. Nat Methods *11*, 677–682.

16. Sailer, A., Anneken, A., Li, Y., Lee, S., and Munro, E. (2015). Dynamic Opposition of Clustered Proteins Stabilizes Cortical Polarity in the C. elegans Zygote. Dev Cell *35*, 131–142.

17. Rodriguez, J., Peglion, F., Martin, J., Hubatsch, L., Reich, J., Hirani, N., Gubieda, A.G., Roffey, J., Fernandes, A.R., St Johnston, D., et al. (2017). aPKC Cycles between Functionally Distinct PAR Protein Assemblies to Drive Cell Polarity. Dev Cell *42*, 400–415.

18. Bailey, M.J., and Prehoda, K.E. (2015). Establishment of Par-Polarized Cortical Domains via Phosphoregulated Membrane Motifs. Dev Cell *35*, 199–210.

19. Hao, Y., Boyd, L., and Seydoux, G. (2006). Stabilization of cell polarity by the C. elegans RING protein PAR-2. Dev Cell *10*, 199–208.

20. Arata, Y., Hiroshima, M., Pack, C.G., Ramanujam, R., Motegi, F., Nakazato, K., Shindo, Y., Wiseman, P.W., Sawa, H., Kobayashi, T.J., et al. (2016). Cortical Polarity of the RING Protein PAR-2 Is Maintained by Exchange Rate Kinetics at the Cortical-Cytoplasmic Boundary. Cell Rep *16*, 2156–2168.

21. Hoege, C., Constantinescu, A.T., Schwager, A., Goehring, N.W., Kumar, P., and Hyman, A.A. (2010). LGL can partition the cortex of one-cell Caenorhabditis elegans embryos into two domains. Curr Biol *20*, 1296–1303.

22. Kumfer, K.T., Cook, S.J., Squirrell, J.M., Eliceiri, K.W., Peel, N., O'Connell, K.F., and White, J.G. (2010). CGEF-1 and CHIN-1 regulate CDC-42 activity during asymmetric division in the Caenorhabditis elegans embryo. Mol Biol Cell *21*, 266–277.

23. Benton, R., and St Johnston, D. (2003). Drosophila PAR-1 and 14-3-3 inhibit Bazooka/PAR-3 to establish complementary cortical domains in polarized cells. Cell *115*, 691–704.

24. Beatty, A., Morton, D.G., and Kemphues, K. (2013). PAR-2, LGL-1 and the CDC-42 GAP CHIN-1 act in distinct pathways to maintain polarity in the C. elegans embryo. Development *140*, 2005–2014.

25. Harris, T.J., and Peifer, M. (2004). Adherens junction-dependent and -independent steps in the establishment of epithelial cell polarity in Drosophila. J Cell Biol *167*, 135–147.

26. Chang, Y., and Dickinson, D.J. (2022). A particle size threshold governs diffusion and segregation of PAR-3 during cell polarization. Cell Reports *39*. 10.1016/j.celrep.2022.110652.

27. Oon, C.H., and Prehoda, K.E. (2019). Asymmetric recruitment and actin-dependent cortical flows drive the neuroblast polarity cycle. Elife *8*.

28. Doerflinger, H., Vogt, N., Torres, I.L., Mirouse, V., Koch, I., Nüsslein-Volhard, C., and St Johnston, D. (2010). Bazooka is required for polarisation of the Drosophila anterior-posterior axis. Development *137*, 1765–1773. 10.1242/dev.045807.

29. Januschke, J., and Gonzalez, C. (2010). The interphase microtubule aster is a determinant of asymmetric division orientation in Drosophila neuroblasts. Journal of Cell Biology *188*, 693–706. 10.1083/jcb.200905024.

30. Rebollo, E., Sampaio, P., Januschke, J., Llamazares, S., Varmark, H., and González, C. (2007). Functionally Unequal Centrosomes Drive Spindle Orientation in Asymmetrically Dividing Drosophila Neural Stem Cells. Developmental Cell *12*, 467–474. 10.1016/j.devcel.2007.01.021.

31. Rusan, N.M., and Peifer, M. (2007). A role for a novel centrosome cycle in asymmetric cell division. Journal of Cell Biology *177*, 13–20. 10.1083/jcb.200612140.

32. Shi, S.-H., Jan, L.Y., and Jan, Y.-N. (2003). Hippocampal Neuronal Polarity Specified by Spatially Localized mPar3/mPar6 and PI 3-Kinase Activity. Cell *112*, 63–75. 10.1016/S0092-8674(02)01249-7.

33. Inaba, M., Venkei, Z.G., and Yamashita, Y.M. (2015). The polarity protein Baz forms a platform for the centrosome orientation during asymmetric stem cell division in the Drosophila male germline. eLife *4*, e04960. 10.7554/eLife.04960.

34. Benton, R., and St Johnston, D. (2003). A conserved oligomerization domain in drosophila Bazooka/PAR-3 is important for apical localization and epithelial polarity. Curr Biol *13*, 1330–1334.

35. Feng, W., Wu, H., Chan, L.N., and Zhang, M. (2007). The Par-3 NTD adopts a PB1-like structure required for Par-3 oligomerization and membrane localization. EMBO J *26*, 2786–2796.

36. Zhang, Y., Wang, W., Chen, J., Zhang, K., Gao, F., Gao, B., Zhang, S., Dong, M., Besenbacher, F., Gong, W., et al. (2013). Structural insights into the intrinsic self-assembly of Par-3 N-terminal domain. Structure *21*, 997–1006.

37. Li, B., Kim, H., Beers, M., and Kemphues, K. (2010). Different domains of C. elegans PAR-3 are required at different times in development. Dev Biol *344*, 745–757.

38. McKinley, R.F., Yu, C.G., and Harris, T.J. (2012). Assembly of Bazooka polarity landmarks through a multifaceted membrane-association mechanism. J Cell Sci *125*, 1177–1190.

39. Dickinson, D.J., Schwager, F., Pintard, L., Gotta, M., and Goldstein, B. (2017). A Single-Cell Biochemistry Approach Reveals PAR Complex Dynamics during Cell Polarization. Dev Cell *42*, 416–434.

40. Wang, S.C., Low, T.Y.F., Nishimura, Y., Gole, L., Yu, W., and Motegi, F. (2017). Cortical forces and CDC-42 control clustering of PAR proteins for Caenorhabditis elegans embryonic polarization. Nat Cell Biol *19*, 988–995.

41. Illukkumbura, R., Hirani, N., Borrego-Pinto, J., Bland, T., Ng, K., Hubatsch, L., McQuade, J., Endres, R.G., and Goehring, N.W. (2023). Design principles for selective polarization of PAR proteins by cortical flows. Journal of Cell Biology *222*, e202209111. 10.1083/jcb.202209111.

42. Lang, C.F., and Munro, E.M. (2022). Oligomerization of peripheral membrane proteins provides tunable control of cell surface polarity. Biophysical Journal *121*, 4543–4559. https://doi.org/10.1016/j.bpj.2022.10.035.

43. Encalada, S.E., Martin, P.R., Phillips, J.B., Lyczak, R., Hamill, D.R., Swan, K.A., and Bowerman, B. (2000). DNA Replication Defects Delay Cell Division and Disrupt Cell Polarity in Early Caenorhabditis elegans Embryos. Developmental Biology *228*, 225–238. 10.1006/dbio.2000.9965.

44. Beers, M., and Kemphues, K. (2006). Depletion of the co-chaperone CDC-37 reveals two modes of PAR-6 cortical association in C. elegans embryos. Development *133*, 3745–3754.

45. Aceto, D., Beers, M., and Kemphues, K.J. (2006). Interaction of PAR-6 with CDC-42 is required for maintenance but not establishment of PAR asymmetry in C. elegans. Dev Biol *299*, 386–397.

46. Munro, E., Nance, J., and Priess, J.R. (2004). Cortical flows powered by asymmetrical contraction transport PAR proteins to establish and maintain anterior-posterior polarity in the early C. elegans embryo. Dev Cell *7*, 413–424.

47. Watts, J.L., Etemad-Moghadam, B., Guo, S., Boyd, L., Draper, B.W., Mello, C.C., Priess, J.R., and Kemphues, K.J. (1996). par-6, a gene involved in the establishment of asymmetry in early C. elegans embryos, mediates the asymmetric localization of PAR-3. Development *122*, 3133–3140.

48. Brenner, S. (1974). The genetics of Caenorhabditis elegans. Genetics *77*, 71–94.

49. Timmons, L., Court, D.L., and Fire, A. (2001). Ingestion of bacterially expressed dsRNAs can produce specific and potent genetic interference in Caenorhabditis elegans. Gene *263*, 103–112.

50. Kamath, R.S., Fraser, A.G., Dong, Y., Poulin, G., Durbin, R., Gotta, M., Kanapin, A., Le Bot, N., Moreno, S., Sohrmann, M., et al. (2003). Systematic functional analysis of the Caenorhabditis elegans genome using RNAi. Nature *421*, 231–237. 10.1038/nature01278.

51. Crocker, J.C., and Grier, D.G. (1996). Methods of Digital Video Microscopy for Colloidal Studies. Journal of Colloid and Interface Science *179*, 298–310. 10.1006/jcis.1996.0217.

52. Jaqaman, K., Loerke, D., Mettlen, M., Kuwata, H., Grinstein, S., Schmid, S.L., and Danuser, G. (2008). Robust single-particle tracking in live-cell time-lapse sequences. Nat Methods *5*, 695–702. 10.1038/nmeth.1237.

53. Huang, W.Y.C., Boxer, S.G., and Ferrell, J.E. (2022). Membrane localization accelerates association under conditions relevant to cellular signaling. 2022.10.22.513358. 10.1101/2022.10.22.513358.